University of Zurich[UZH]

Master thesis

Search for radiation from wave function collapse and electric field characterization in XENONnT

Livio Redard-Jacot

Supervisors
Prof. Dr. Laura Baudis
Dr. Christian Wittweg

Zurich, October 23, 2022

Abstract

This thesis reports on a search for spontaneous radiation from wave function collapse in the first science data from XENONnT. It further investigates the impact of the inhomogeneous electric drift field in the detector. Based on the results of a performed data-driven reconstruction of the drift field, it was found that the corresponding field corrections are of the order of 0-2% and subdominant compared to other signal corrections. With this, the search for x-ray signatures of spontaneous wave function collapse was performed in the parameter space of reconstructed event energy using the analysis framework developed for the XENONnT low-energy electronic recoil searches. No evidence of such a signal was found in 1.16 tonne-years of exposure. Given the low electronic recoil background in the energy region of interest (19, 140) keV, this allowed to set limits on the phenomenological parameters of the continuous spontaneous localization (CSL) and Diósi-Penrose (DP) models. We obtain $\lambda/r_c^2 < 3.04 \times 10^{-3}$ $\mathrm{s}^{-1}\mathrm{m}^{-2}$ at 95% C.L. for the CSL model and $R_0 > 1.4 \times 10^{-9}$ m at 95% C.L. for the DP model. These represent the first results from a liquid xenon TPC and set the strongest upper bounds on the CSL model for $r_c < 10^{-5}$ m and the strongest bounds on the DP model to date.

Contents

Introduction

> There is a difference between a blurred or poorly focused photograph and a photograph of clouds and wafts of mist.
>
> Erwin Schrödinger, 1935

The theory of quantum mechanics has revolutionized our understanding of Nature at small scales and predicts the outcomes of experiments with great success. However, since its development over 100 years ago, the theory has sparked a debate about the measurement process itself that has yet to be resolved. It is not the complexity of such a process that is not understood but the fundamental difference between the dynamics of a quantum system before and during a measurement. Whereas quantum systems can be in superposed states, we always observe only one state at the time of measurement. And although the Schrödinger equation, which describes the dynamics, is deterministic, it can only assign a probability to a quantum mechanical system being found in a specific state. This constitutes the measurement problem.

The models of wave function collapse offer a possible solution to this problem [1]. By modifying the Schrödinger equation, these models add an internal mechanism to the theory that causes the breakdown of superposition without the need for an external observer. Moreover, the mechanism is intrinsically probabilistic. To preserve the successful description of quantum mechanics of the microscopic world, the introduced collapse mechanism only becomes dominant for large systems. Thus, models of wave function collapse are phenomenological theories, suggesting that there is a more fundamental underlying theory.

Due to the modified dynamics, the predictions of the models of wave function collapse deviate from standard quantum mechanics and thus can be tested experimentally [2]. One consequence of the collapse mechanism is the diffusion of particles in space, resulting in the emission of radiation for charged particles. The radiation is predicted

to be emitted predominantly in the x-ray regime at a low rate, requiring detectors with a low background and an energy threshold at the keV scale. Several experiments have tried to detect the radiation, but so far, without success. Nevertheless, they were able to constrain or rule out certain subsets of proposed wave function collapse models.

This work presents the first search by the XENONnT dark matter experiment for the radiation from wave function collapse. The main goal of the experiment is the direct detection of dark matter in the form of weakly-interacting massive particles via their interaction with xenon nuclei [3]. However, the low background and the large target mass make the detector a leading observatory for various other rare event searches [4]. For this thesis, I use the data collected during the first science run between July and November 2021 to test two of the most studied wave function collapse models: the continuous spontaneous localization model [5] and the Diósi-Penrose model [6]. Both models predict a collapse-induced radiation emission by charged particles.
The expected signal of both models is continuous in energy. This motivates a good understanding of the detector's signal reconstruction over a broad range of energies. XENONnT detects scintillation and ionization signals generated by particle interactions with xenon electrons or nuclei. To measure the ionization, an external electric field is required to drift electrons away from the interaction site to a gaseous phase above liquid xenon, where they induce a secondary scintillation light. However, this electric drift field is not completely uniform. Therefore, before performing the signal search, I reconstruct the electric drift field with a data-driven approach. I use the results to investigate how the non-uniformity of the drift field affects the signal reconstruction and consequently the search for radiation from wave function collapse.

The thesis is structured as follows: Chapter 1 introduces the theoretical motivation for wave function collapse models, outlines how they can be tested experimentally, and gives an overview of the current state of research. Chapter 2 describes the design, the detection principle, and the signal reconstruction of the XENONnT experiment. The reconstruction and characterization of the electric drift field are presented in chapter 3. The method and results of the search for radiation from wave function collapse are shown in chapter 4, followed by a conclusion and an outlook.

Chapter 1

Wave function collapse

The models of wave function collapse, or just collapse models, were introduced to explain the absence of superposition of macroscopic objects and the probabilistic nature of measurements in quantum mechanics. Before presenting different proposed collapse models, the measurement problem of quantum mechanics is explained in more detail in the following section.

1.1 The measurement problem of quantum mechanics

The measurement problem already became apparent in the beginnings of quantum mechanics, most famously illustrated by Erwin Schrödinger's cat paradox [7]. The absurd thought experiment of a cat being alive and dead at the same time before observing it highlights the special role of the measurement and the fact that the theory does not set an upper limit at which it is no longer valid. Why does the cat behave classically and not quantum-like when it is made of atoms? The apparent lack of macroscopic superposition contradicts the superposition principle that follows directly from the linearity of the Schrödinger equation.
The standard formulation of quantum mechanics postulates that the wave function collapses to one eigenstate of an observable as a consequence of the measurement process [8]. An idealized measurement scheme by von Neumann illustrates why this axiom is problematic [9]. A derivation without assuming an idealized measurement is given here [10] but leads to the same conclusion. The spin of a single electron is measured in a certain direction. The wave function $|\varphi_0\rangle$ describes the initial configuration of the

electron that forms a superposition of the spin pointing up- and downwards:

$$|\varphi_0\rangle = \frac{1}{\sqrt{2}} \left(|up\rangle + |down\rangle \right). \tag{1.1}$$

The macroscopic measuring apparatus A has two disjoint pointer states A_1 and A_2 that correspond to the two spin eigenstates. Even though the macroscopic apparatus has many degrees of freedom, it is in principle described by a wave function if quantum mechanics is a complete theory. Interacting with the electron, the system evolves according to the linear Schrödinger equation into the following entangled final state:

$$|\varphi_0\rangle \otimes |A_0\rangle \quad \longrightarrow \quad \frac{1}{\sqrt{2}}(|up\rangle \otimes |A_1\rangle + |down\rangle \otimes |A_2\rangle). \tag{1.2}$$

If the wave function contains all the information about the electron as well as the macroscopic apparatus, and the time evolution is strictly linear, then the measurement itself cannot destroy superposition. Due to the linear interaction, the apparatus is in a state of macroscopic superposition in the final state. This is of course not what is observed: Individual measurements show the spin directed up- or downward.
This leads to the second aspect of the measurement problem, the emergence of probabilities in quantum mechanics. By the Born rule, the square modulus of the wave function can be interpreted as probability for the occurrence of each outcome, e.g. in 1.2 both spin directions are equally probable. The rule gives accurate predictions for experiments but stands in strong contrast to the Schrödinger equation's deterministic nature. For a given initial state of the wave function, the equation determines how it evolves over time. In essence, the measurement problem raises the crucial question if quantum mechanics provides a fundamental description of nature or if it is just a method to predict the outcomes of measurements [11].
Several resolutions to the measurement problem have been proposed, though none has gained consensus or been proven correct. The three main proposals can be presented along three incompatible assumptions of standard quantum mechanics, following [12]:

1. The wave function gives a complete description of a physical system.
2. The time evolution of the wave function is always determined by the linear Schrödinger equation.
3. Measurements yield definite outcomes.

Each proposal has to reject one of these assumptions to resolve the measurement problem. Thereby, the first two proposals do not change the predictions for experiments and therefore are not falsifiable.

- The **de Broglie-Bohm theory** rejects the first assumption and hence is a so-called hidden-variables theory [13]. At the center of the theory are point particles that move along trajectories determined by the wave function. However, the initial conditions are in principle unknown or hidden.

- In **the Many-worlds interpretation** introduced by Everett, measurements do not result in one or another outcome, but instead all possible outcomes are realized by splitting up the Universe into independent branches [14].

- **Collapse models** reject the second assumption by proposing new physics, but retain the assumption of definite outcomes in measurements and a complete description of a physical system by the wave function.

1.2 Wave function collapse models

Over the last decades, a variety of collapse models have been developed [1]. They all incorporate a modified Schrödinger evolution that breaks the quantum superposition at the transition from the microscopic to the macroscopic realm. The mathematical description of the new dynamics replaces the collapse postulate of the Copenhagen interpretation and makes the role of the external observer obsolete. Besides substantial differences, the collapse models share many common features that are necessary for a coherent solution to the measurement problem: The additional terms in the Schrödinger equation are nonlinear to suppress superposition. They are stochastic, so the collapse to an eigenstate is random but distributed according to the Born rule, and they must prohibit faster-than-light signaling to preserve causality. Furthermore, an amplification mechanism is required that makes the new terms only dominant when the size or mass of systems increases. Finally, the localization of the wave function occurs in the position basis to ensure that no macroscopic object is found delocalized in space.
The first consistent collapse model that was able to fulfill all these properties was the GRW model, introduced by Ghirardi, Rimini, and Weber (GRW) in 1986 [15]. Its simple collapse mechanism is illustrated in figure 1.1 and conveys the general idea of collapse models well. Each particle in an N-particles system experiences collapses, also called jumps, that occur randomly in time and space. The spontaneous jumps localize not only the wave function of the single particle but of the whole N-particle system and are represented by a Gaussian operator L. The position distribution of the jumps is given by $||L_x^i \ \psi(x_1, ..., x_n, t)||^2$ such that the localization coincides with standard quantum mechanics. Between jumps, the evolution of the wave function follows the

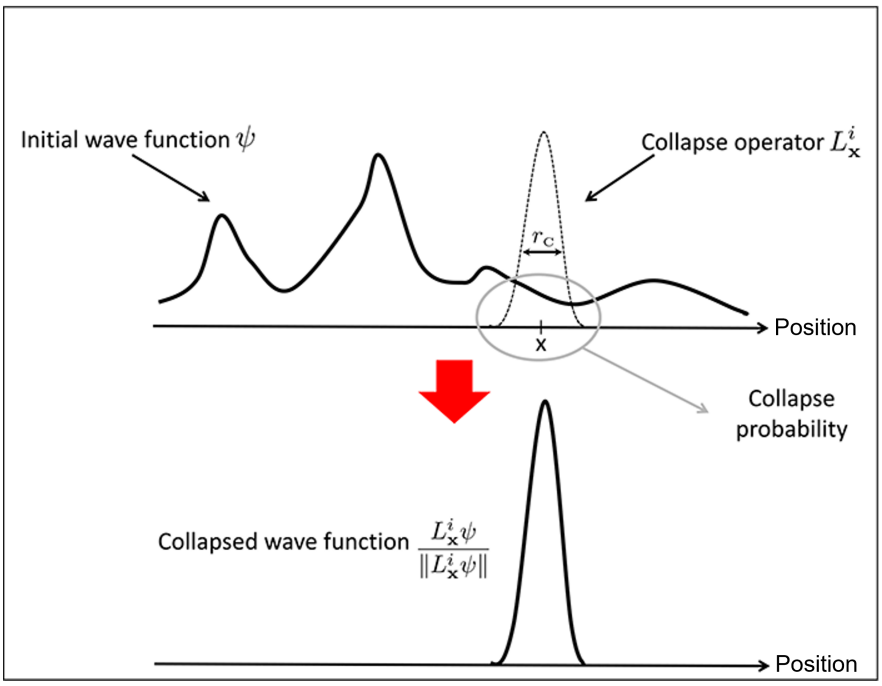

Figure 1.1: Schematic of the waveform collapse process in the GRW model in 1D. The initial wave function ψ is localized in space by the multiplication with a Gaussian function. The larger the wave function at a given position, the larger is the collapse probability. The final state has a resolution r_c. Figure adapted from [11].

standard Schrödinger equation. The model has two phenomenological parameters that need to be determined experimentally: the mean collapse rate λ determining the frequency of jumps, and the resolution r_c setting the spatial width of the collapse.
The GRW model was subsequently developed further to replace the discrete jumps with a continuous evolution and to include the description of identical particles. In the focus of this work are two of the most studied collapse models, the continuous spontaneous localization model and the Diósi-Penrose model.

1.2.1 Continuous spontaneous localization model

The continuous spontaneous localization (CSL) model is a continuous generalization of the GRW model, including the description of identical particles [5]. The jumps are replaced by a continuous collapse process that is induced through the interaction between particles and a randomly fluctuating classical field. The random field, or noise field, is primarily introduced to describe the stochasticity of the collapse process. However, it has been suggested that the field could be interpreted as a real physical field, possibly

of cosmological origin [1]. The continuous interaction of particles with the noise field does not only localize the wave function but induces a Brownian-like diffusion of the particles, corresponding to an accelerated movement in space. In the case of charged particles, the random acceleration leads to the spontaneous emission of radiation. The diffusion and the resulting radiation are not predicted by quantum mechanics and offer the opportunity to test the CSL model, as it will be discussed in section 1.3 in more detail.
The modified Schrödinger dynamics can be expressed in terms of a stochastic differential equation [16]:

$$\mathrm{d}\,|\psi_t\rangle = \Big[-\frac{i}{\hbar}\hat{H}\;\mathrm{d}t + \sqrt{\alpha}\int \mathrm{d}^3\mathbf{x}\left(\hat{M}(\mathbf{x}) - \langle\hat{M}(\mathbf{x})\rangle_t\right)\mathrm{d}W_t(\mathbf{x}) \\ -\frac{\alpha}{2}\int \mathrm{d}^3\mathbf{x}\;\mathrm{d}^3\mathbf{y}\;\mathcal{D}(\mathbf{x}-\mathbf{y})\prod_{\mathbf{q}=\mathbf{x},\mathbf{y}}\left(\hat{M}(\mathbf{q}) - \langle\hat{M}(\mathbf{q})\rangle_t\right)\mathrm{d}t\Big]\,|\psi_t\rangle\,, \quad (1.3)$$

where $|\psi_t\rangle$ is the wave function in standard bracket notation, and $\mathbf{x}$ and $\mathbf{y}$ are 3D spatial vectors. The first term on the right side of eq. (1.3) represents the standard Hamiltonian evolution, dominating the microscopic regime. The second and third term cause the localization in space. The stochastic dynamics is expressed in the form of Wiener processes $W_t(\mathbf{x})$ for each point in space [17]. The noise field is then defined as $w_t(\mathbf{x}) = dW_t(\mathbf{x})/dt$ and has the correlation function $\mathcal{D}(\mathbf{x}-\mathbf{y})$ given by

$$\mathcal{D}(\mathbf{x}-\mathbf{y}) = \exp\left(-|\mathbf{x}-\mathbf{y}|^2/4r_{\mathrm{C}}^2\right). \quad (1.4)$$

The collapse operator is the mass density operator $\hat{M}(\mathbf{x}) = m\psi^\dagger(\mathbf{x})\psi(\mathbf{x})$, with the particle creation and annihilation operators $\psi^\dagger(\mathbf{x})$ and $\psi(\mathbf{x})$. The non-linearity is introduced by the expectation value of $\hat{M}(\mathbf{x})$:

$$\langle\hat{M}(\mathbf{x})\rangle_t = \langle\psi_t|\hat{M}(\mathbf{x})|\psi_t\rangle. \quad (1.5)$$

The characteristic constant of the model is

$$\alpha = \frac{\lambda}{m_0^2}, \quad (1.6)$$

where the mass m_0 is a reference mass that is by convention set equal to the nucleon mass. The phenomenological parameters are the same as in the GRW model, the collapse rate λ and the resolution or correlation length r_c. The two parameters define at which scale the collapse terms become dominant and suppress macroscopic superposition. In this reasoning, Ghirardi, Rimini and Weber proposed $\lambda_{GRW} = 10^{-16}\ \mathrm{s}^{-1}$ and

$r_c = 10^{-7}$ m [15]. Later, Adler argued that collapse should already be effective in the mesoscopic regime, based on the process of latent image formation, where relatively few particles form a photography. Adler proposed to set $\lambda_{Adler} = 4 \times 10^{-8\pm2}$ s^{-1} at $r_c = 10^{-7}$ m or $\lambda_{Adler} = 10^{-6\pm2}$ s^{-1} at $r_c = 10^{-6}$ m [18].
The CSL model gives a consistent framework of the collapse, but two problems arise from it. First, the Brownian diffusion induced by the noise field clearly violates energy conservation. It increases the energy of the system slowly but steadily. A possible resolution are dissipative extensions of the model, where the energy reaches a finite equilibrium [19]. Second, the noise field of the CSL model is white in time, meaning it has a flat frequency spectrum. This is a mathematical idealisation and can not represent a real physical field. Colored extensions have been formulated, where the noise field has a frequency cutoff as a new parameter [20].
The mentioned modifications of the CSL model preserve the collapse process but can alter the predictions for empirical tests. Besides the extensions, there is also an ongoing effort to develop an underlying fundamental theory from which the collapse models emerge and that could resolve these problems [21]. Such a theory would also provide a stronger theoretical motivation for the phenomenological collapse models.

1.2.2 Diósi-Penrose model

The Diósi-Penrose (DP) model emerged from the idea that the collapse of the wave function could be caused by gravity [6, 22]. The larger the mass of a system, the faster is the collapse of the superposition of different spacetimes. Like the CSL model, the general structure can be expressed in terms of eq. 1.3 with [2]

$$\mathcal{D}_{\mathrm{DP}}(\mathbf{x}-\mathbf{y}) = \frac{1}{|\mathbf{x}-\mathbf{y}|} \tag{1.7}$$

$$\alpha_{\mathrm{DP}} = \frac{G}{\hbar}, \tag{1.8}$$

where $\mathcal{D}_{\mathrm{DP}}(\mathbf{x}-\mathbf{y})$ is the correlation function of the DP model and G in α_{DP} is the gravitational constant. In addition, a parameter R_0 needs to be introduced to give particles a finite size. For point-particles, the collapse rate diverges and the instantaneous collapse would suppress superposition also for microscopic systems. Penrose, who developed the gravity-related collapse model independently from Diósi, suggested to set the regularization parameter R_0 equal to the spatial width of the wave function [23]. The similar structure of the CSL model and the DP model imply that the gravity-related model also induces a Brownian diffusion that can be probed experimentally.

1.3 Experimental tests

There are two approaches to test the CSL model and the DP model: interferometric and non-interferometric experiments. No type of experiment has observed a conclusive signal so far, but technological improvements have made it possible to constrain the corresponding parameter spaces more and more.

1.3.1 Interferometric experiments

The most direct way to check the validity of the superposition principle at all scales is to demonstrate that even large, massive particles show interference effects [24]. The challenge in interferometric experiments lies in preparing a well-isolated system where a coherent spatial superposition persists over a long enough period of time. Otherwise, the interaction with the environment destroys the interference. Note here, that decoherence by environmental interactions can, however, not resolve the measurement problem. Decoherence disentangles superposed states but cannot destroy the superposition [1]. The most stringent interferometric limit for the CSL model was set by an experiment that measured interference fringes for molecules consisting of up to 2000 atoms and with masses above 25 kDa [25]. The experiment excluded collapse rates $\lambda > 10^{-7}$ s^{-1} at $r_c = 10^{-7}$ m and thus parts of the theoretical values suggested by Adler [18]. Interferometric experiments are not the most sensitive test of the CSL model, but they are robust to dissipative and colored modifications of the model (see sec. 1.2.1) [26]. For the DP model, interferometric experiments have not been able to set competitive limits [27].

1.3.2 Non-interferometric experiments

Non-interferometric experiments try to measure the Brownian diffusion induced by the noise field. The approach has the advantage that the system under investigation does not need to be in a carefully prepared superposed state. A variety of experimental techniques can exploit the continuous interaction of particles with the noise field, described briefly below. Figure 1.2 displays the most stringent exclusion limits for the CSL model from non-interferometric experiments and theoretical propositions.

Cold atoms

Cold atom experiments cool a few atoms down to temperatures near absolute zero. They can then measure the position variance of the cloud of atoms. The collapse-induced Brownian diffusion would give rise to additional growth of the position variance

compared to the quantum mechanical prediction [28]. If no excess growth is observed, this type of experiment can set upper limits on the CSL collapse parameters. These limits are almost unaltered for colored CSL models. For dissipative models, however, they are much weaker because the dissipative effect reduces the Brownian diffusion.

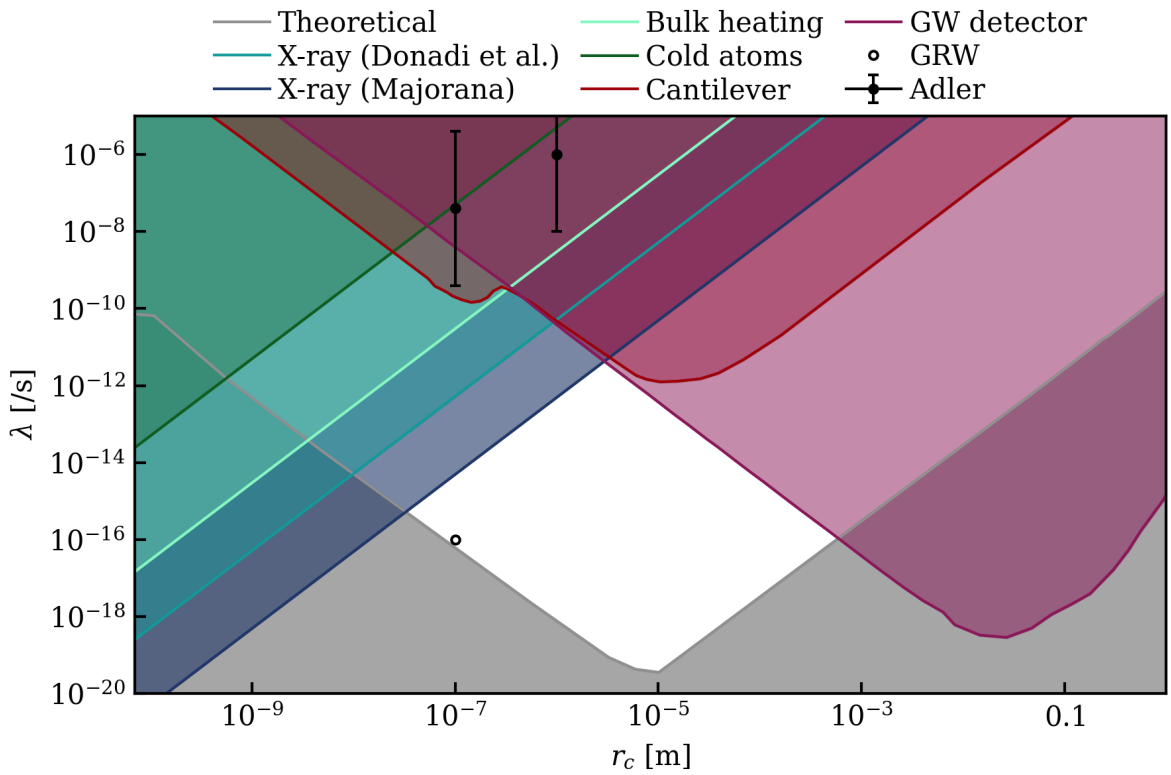

Figure 1.2: Exclusion limits for the CSL collapse parameters λ and r_c from non-interferometric experiments and theoretical propositions. The upper bound from the gravitational wave (GW) detector LISA Pathfinder [29, 30] excludes the purple shaded parameter space. The red exclusion area is obtained from a cantilever experiment [31], the green area from a cold atoms experiment [28], and the blue-green area is derived from the measured heating rate in the CUORE experiment [32]. The two most stringent limits from searches for x-ray emission are set by Donadi et al. [33] (light blue) and the MAJORANA experiment (dark blue) [34]. The black dots and the circle represent the theoretical values suggested by Adler [18] and GRW [15], respectively. The theoretical lower bound excluding the gray area is based on the following requirement: a graphene disk of the minimum size a human eye can resolve ($\simeq$ 0.01 mm) should be localized faster than the human eye's perception time ($\simeq$ 10 ms) [26]. The white area is the parameter space not yet excluded.

Bulk heating

Similarly, the increase in kinetic energy can be measured in terms of the heating rate of a bulk material at a low temperature. To test the collapse model, the measured heating rate is compared to the predicted energy depositions of radioactive decays and muons. The neutrinoless double-beta ($0\nu\beta\beta$) decay experiment CUORE [32] has set the most stringent upper limit of this kind and can exclude λ_{Adler} completely [35]. Tellurium dioxide crystals serve as the bulk material and are held at temperatures around 10 mK.

Optomechanical systems

In Optomechanical systems, a mechanical resonator interacting with a radiation field is used to measure the motion of an object with extremely high precision. The environment as well as the noise field affect the motion of a test mass. Cantilevers are one type of mechanical resonator that has been used to constrain the CSL model [31]. Another type of optomechanical systems are gravitational wave detectors. The space-based LISA Pathfinder provides the most stringent limit on the collapse rate λ for $r_c > 10^{-5}$ m [29]. The detector measures the motion of two approximately free-falling masses with an optical system. In contrast to cantilevers, gravitational wave detectors can also set significant constraints on the DP model. LISA Pathfinder excludes regularization scales $R_0 < 4.01 \times 10^{-14}$ m and thus of the size of a nucleon [30, 36].

X-ray emission

Apart from measuring the Brownian diffusion directly, experiments can search for its secondary effect, the spontaneous radiation emission by electrically charged particles. The main component of these detectors is a target material that can detect the collapse induced radiation via electromagnetic interactions but serves at the same time as emitter of the radiation. The emission rate is the largest in the x-ray regime, what will be explained in chapter 4. To be sensitive to this signal, the detectors need to have an energy threshold at the keV scale and a low background. This is achieved by direct detection dark matter experiments and $0\nu\beta\beta$ decay experiments. The background in these experiments originates from radioactive decays in detector components, the target material and the environment, as well as from cosmic particles depositing energy within the detector. To reduce it, the detectors are designed to minimize the radioactive contamination of their components and are located deep underground, where they are partially shielded from cosmic rays.
For the CSL model, the search for x-ray emission currently sets the most stringent constraints for correlation lengths of $r_c < 10^{-6}$ m. Both upper limits shown in fig. 1.2 are

obtained with $0\nu\beta\beta$ decay experiments employing high-purity germanium crystals [33, 34]. On the downside, the introduction of a frequency cutoff by colored CSL models has a substantial impact on the predicted radiation emission rate. A physical noise-field of cosmological origin with a cutoff around 10^{12} s^{-1} would make the radiation completely inaccessible for the two shown experiments [37].
For the DP model, the theoretical emission rate is similar. The MAJORANA DEMONSTRATOR (MAJORANA) experiment has set the strongest lower limit on R_0, excluding values below 4.94×10^{-10} m. The result rejects Penrose's hypothesis that relates R_0 to the spatial width of the wave function [38]. It follows that R_0 cannot be identified with the size of a particles mass density and the parameter has to be left free and can only be determined experimentally.
Direct detection dark matter experiments have not presented results for this search yet. The most sensitive detectors of this kind are dual-phase time projection chambers as employed, for example, in the XENONnT experiment.

Chapter 2

The XENONnT experiment

XENONnT is a direct detection dark matter experiment using a dual-phase time projection chamber (TPC) as a detector. It measures the scintillation and ionization signals of particle interactions within the xenon target [3]. The experiment is located underground at the INFN Laboratori Nazionali del Gran Sasso (LNGS) in Italy, at an average depth of 3.6 km water equivalent. It is an enlarged and improved version of its predecessor, the XENON1T experiment, from which it reuses several subsystems [39]. Like XENON1T, it is designed to directly measure interactions of dark matter with atomic nuclei.

The existence of dark matter is motivated by astrophysical and cosmological observations at all scales [40]. From measurements of rotation curves of galaxies, observations of gravitational lensing to the cosmic structure formation, they all show that baryonic matter interacts via gravity with an unknown type of matter called dark matter. The study of the cosmic microwave background indicates that 84% of the total matter density in the Universe is in the form of dark matter. However, its fundamental nature is unknown and one of the great puzzles in physics today.

The evidence suggests that dark matter could be formed by a new particle beyond the Standard Model [41]. Such a dark matter particle would have to be massive, should only interact gravitationally and eventually weakly, and its abundance should be consistent with the abundance of dark matter. A well-motivated candidate fulfilling these requirements is the weakly interacting massive particle (WIMP) that emerges from theoretical extensions of the Standard Model, such as Supersymmetry. WIMPs are predicted to scatter on an atomic nucleus, transferring a small amount of energy, but only very rarely. Thus, to detect WIMPs directly, an experiment has to have a large target mass and measurement time (exposure), a low energy threshold and a low background. The realization of these requirements in XENONnT makes the detector ideal for other rare event searches, such as the search for radiation from wave function

Figure 2.1: XENONnT experiment with the water tank (left), cooling and purification systems and data read-out infrastructure (right) located underground. Image credit: XENON collaboration.

collapse. In the following, the design of the XENONnT detector and its subsystems with regard to the experimental requirements is introduced.

2.1 Experimental design

Before the XENONnT experiment was built, all used construction materials were carefully selected to minimize their contribution to the background. In a radioassay campaign material samples were screened to measure their radioactive contamination [42]. These measurements are also important later on to model the material background for a signal search.

The experiment consists of multiple subsystems depicted in figure 2.1. Next to the large water tank containing the detector, there is a support building where the xenon is cooled, purified and stored, and the data acquisition (DAQ) system is located. The cooling system keeps the xenon liquefied at a constant temperature of 177 K. Different purification systems remove radioactive contaminants from the xenon. A dominant contribution to the background originates from ^{214}Pb that is in the decay chain of ^{222}Rn, which is continuously emanated from detector materials. A dedicated radon removal system reduces the concentration of ^{222}Rn to 1.7 µBq/kg via continuous cryogenic

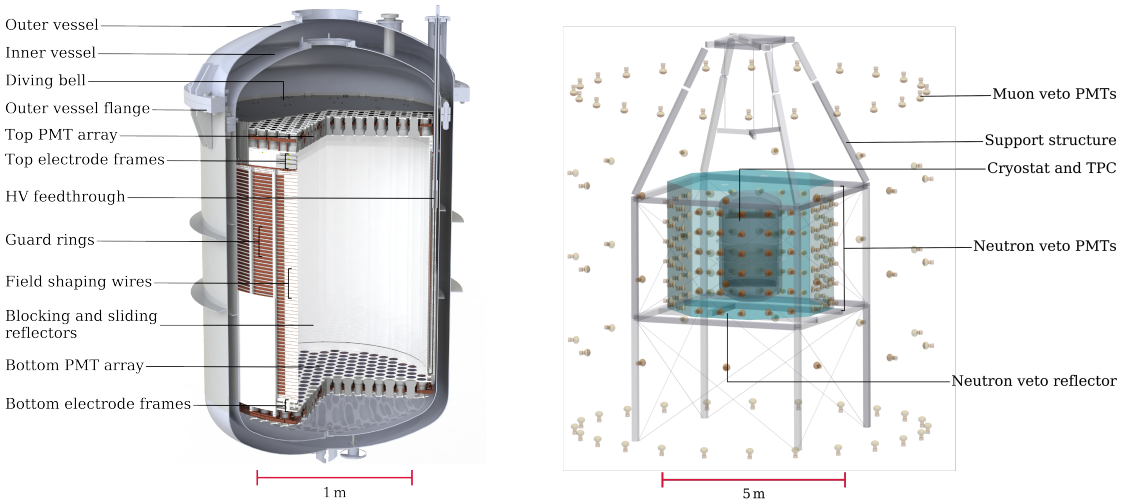

(a) **(b)**

Figure 2.2: a) Sketch of the XENONnT dual-phase TPC enclosed by a double-walled stainless-steel cryostat and b) of the three nested detectors. Both figures from [3].

distillation [43]. A Krypton distillation column is installed to remove ^{85}Kr, another important background source [44]. In addition, the xenon is circulated through rare-gas purifier filters to remove electronegative impurities such as water and oxygen. These contaminants attenuate the ionization and scintillation signals [39].

The sketch in fig. 2.2b illustrates the inside of the water tank. The water does not only shield the detector from radioactivity of the environment but serves at the same time as an active water Cherenkov muon veto. 84 photomultiplier tubes (PMTs) of 8-inch are mounted to the tank's walls to measure the Cherenkov light generated by cosmic muons passing through the water [45]. Optically separated from the muon veto, there is a neutron veto made of reflective panels and 120 8-inch PMTs to measure the signals originating from neutron captures in the water.

At the core of the experiment is the dual-phase TPC illustrated in fig. 2.2a, where particles interact with the liquid xenon and deposit energy. It is installed in the middle of the neutron veto and is enclosed by a double-walled stainless-steel cryostat to thermally insulate it. The cylindrical TPC has a diameter of 1.3 m and a height of 1.5 m. It is filled with 5.9 t of liquid xenon (LXe) and has a gaseous phase of xenon (GXe) on top. Two arrays of 3-inch PMTs ([46]) detect the light signals from interactions, 253 at the top and 241 at the bottom. The TPC walls are made of Polytetrafluoroethylene (PTFE) reflective panels to maximize the amount of collected light. Electrodes and field-shaping wires are used to apply an electric drift field in the liquid and an extraction field in the gaseous phase. The two electric fields are required for the detection

method of a dual-phase TPC, introduced in the following section.

2.2 Signal detection with a dual-phase TPC

An incident particle deposits energy either on a xenon nucleus, denoted as nuclear recoil (NR), or on a bound electron, an electronic recoil (ER). Both interactions generate excitation, ionization, and heat. The share of each process varies with the type of interaction [47]. Figure 2.3 illustrates how the dual-phase TPC can detect the excitation and the ionization signal. The excited xenon atoms $Xe^{\star}$ rapidly form excited dimers $Xe_2^{\star}$ with neighboring xenon atoms. The dimers decay to the dissociative ground state by emitting scintillation light at 175 nm in the vacuum UV regime [48]. In addition, the ions Xe^{+} and free electrons e^{-} produced by ionization can recombine to a dimer, releasing more light. These two mechanisms give rise to the prompt scintillation signal that is detected by the PMTs and called S1. A secondary delayed signal is created with the help of the electric drift field, that is applied between the cathode, above the

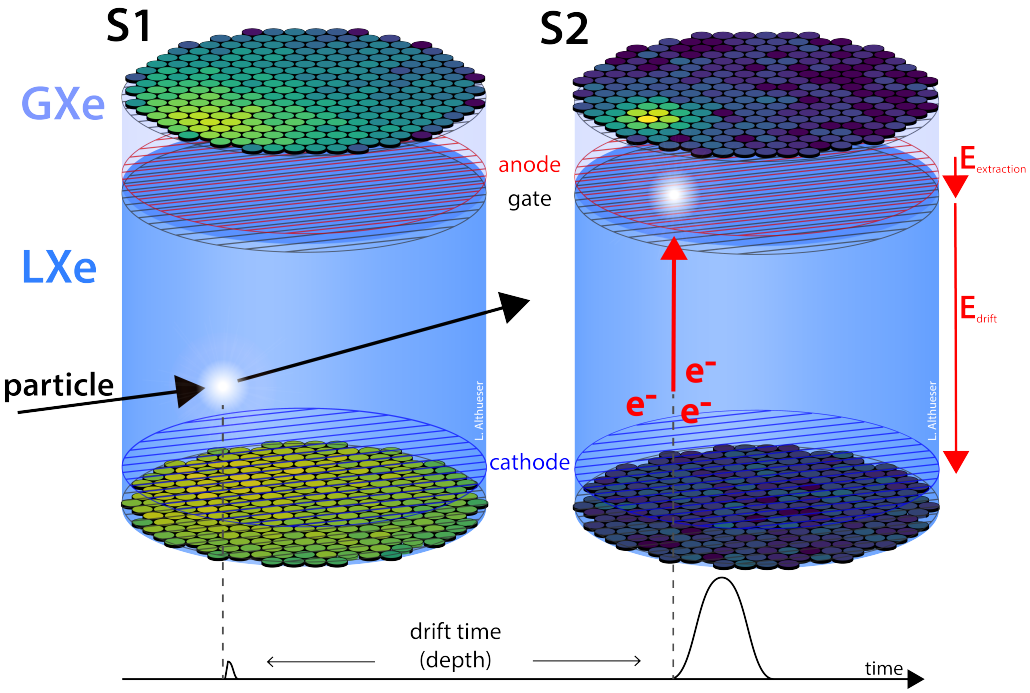

Figure 2.3: Signal detection in a dual-phase xenon TPC. The energy deposition of a particle creates a prompt scintillation light (S1) and free electrons that create a delayed secondary light signal (S2) when they are extracted into the gaseous phase. The two light signals are detected by two arrays of photosensors. Image credit: Lutz Althueser.

bottom PMTs, and the gate, slightly below the gaseous phase. The drift field suppresses the recombination process and drifts ionization electrons upwards within the liquid. The strong electric field of a few kV/cm between gate and anode extracts them into the gaseous phase producing scintillation light via electroluminescence, also at 175 nm. This amplified signal is called S2 and is proportional to the number of electrons. Both S1 and S2 are given in the unit of photoelectrons (PE), the number of electrons ejected at the PMT photocathodes.
With the two signals, the position and energy of an interaction can be reconstructed [49]. The horizontal position (r,φ) of an event is determined from the S2 light pattern on the top PMT array. The drift time between the prompt S1 and the delayed S2 signal gives the vertical position (z). To determine the total deposited energy per event, both S1 and S2 are combined. The ratio of S1 to S2 depends on the type of interaction and the energy, but they are anti-correlated such that the energy can be calculated from their weighted sum [39]:

$$E = W\left(\frac{S1}{g_1} + \frac{S2}{g_2}\right), \tag{2.1}$$

where W=13.7 eV is the average energy to ionize or excite a xenon atom, and S1 and S2 are the signals in PE. The photon detection efficiency g_1 describes the average amount of measured PE per scintillation photon, the charge amplification factor g_2 per escape electron, respectively. The two parameters are detector-specific and measured with radioactive calibration sources that generate a mono-energetic signal. Figure 2.4 shows the fit of such an energy calibration in XENONnT.
A crucial advantage of the presented detection principle is that it enables a significant reduction of the background in three different ways. First, electronic recoils can be distinguished from nuclear recoils by their ratio S1/S2, because they generate relatively more ionization [47]. The discrimination allows to reject ER interactions, for example β and γ decays, as a background in an NR signal search, and vice versa. Second, the 3D position information can be used to select only interactions occurring in the central volume of the TPC, the fiducial volume. The liquid xenon in the outer parts shields the fiducial volume very effectively from external radioactivity of detector materials and the environment. Finally, events with multiple interactions inside the TPC, such as they would occur for neutrons or Compton-scattered γ-rays, can be removed for searches of signals that interact only once [49].

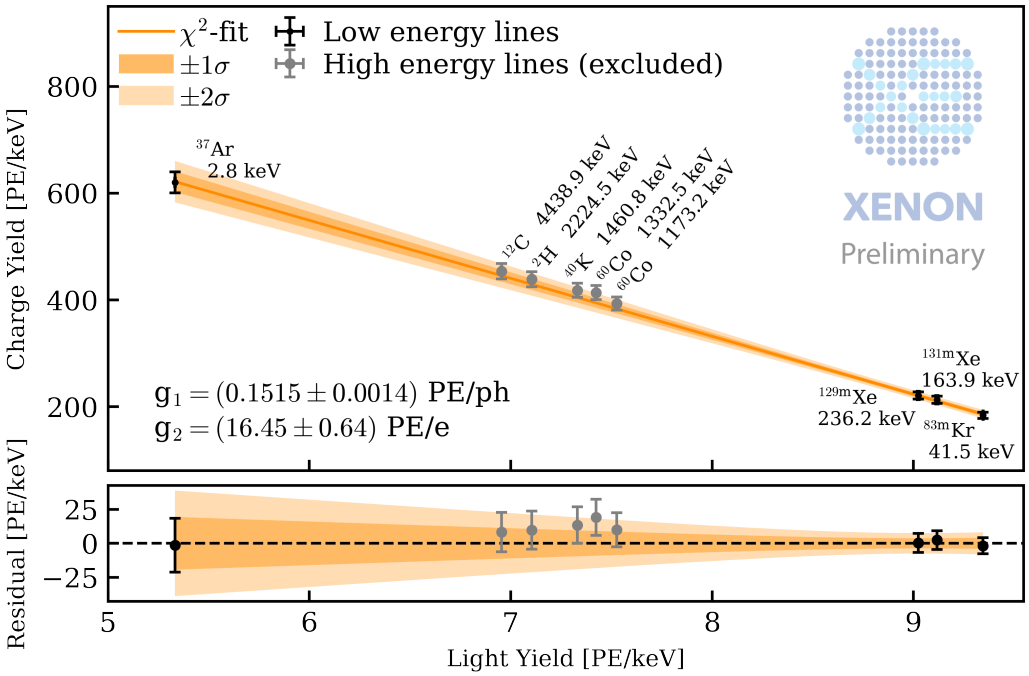

Figure 2.4: Top panel: Energy calibration of XENONnT extracted from the charge yield per unit energy as a function of the light yield per unit energy. Black markers denote mono-energetic calibration lines used for a fit of g_1 and g_2. Grey points from high energy lines above 1 MeV were excluded from the fit due to missing high-energy optimizations. The best-fit calibration is indicated by a solid orange line. The 1σ and 2σ uncertainty bands from uncertainty propagation with the covariance matrix are indicated by the darker and lighter orange bands, respectively. Bottom panel: Non normalized residuals of the fit with model uncertainties. Figure from [50].

2.3 Event reconstruction

When the PMTs of a dual-phase TPC detect scintillation light, they convert it into electrical signals, which are then digitized and saved as raw data. For analysis, the raw data has to be processed to reconstruct the individual interactions and their corresponding S1 and S2 signals. In XENONnT, this event reconstruction process is done with the software straxen [51].

Straxen is is used for the processing, storage and corrections of the collected data. It is built on top of strax [52], a generic analysis framework for xenon TPC experiments. The framework consists of four basic structures: the context, plugins, data types and data kinds. The context holds the general configuration of the processing. The plugins are the algorithms that produce different data types. The data types are defined by the specific information they contain. The data kinds represent different levels of the

data processing.
In straxen, there are five data kinds corresponding to five main levels of the reconstruction process [53]: pulses, hits, peaklets, peaks and events. The digitized and amplified signals of the PMTs are called pulses and form the lowest level. When XENONnT collects data, the data acquisition system records all pulses that crossed the internal trigger level of a PMT channel. The pulses are stored for each PMT individually at this stage. In the next step, an algorithm identifies hits. These are defined as pulses that are above a certain threshold and occur within a certain time window.
The goal is then to identify peaks from the hits that correspond to individual S1 or S2 signals. To do so, the hits from different PMTs occurring within 700 ns are grouped into clusters [4]: the peaklets. The peaklets are divided into smaller clusters until they contain no more than one S1 or S2 candidate. The peaklets are represented by so-called waveforms, the sum of all contributing pulses as a function of the time. By integrating a waveform over time, the number of measured photoelectrons is obtained, denoted as peak area. Based on the rise time, width and area of the waveform, and the number of contributing PMTs, the peaklets can be classified as S1 or S2 peaks. While S1 peaks have a fast-rising waveform, the S2 peaks are broader due to the diffusion of the electron cloud during the drift and the extraction process that generates the secondary scintillation. S1 peaks need at least three PMTs contributing within a time window of 100 ns, S2 peaks require at least four contributing PMTs.
To obtain events corresponding to an interaction inside the TPC, the S1 and S2 peaks are paired. The pairing algorithm starts with an S2 peak above 100 PE and defines a time window around it. In multiple steps, a matching S1 is searched. As some interactions, such as a decay, deposit energy in two stages at the same position, a second S1 or S2 peak can be added to a paired S1 and S2 peak. The larger peaks are denoted as main S1 and S2 and the smaller ones as alternate S1 or S2. Figure 2.5 shows the waveform of a successful pairing of an S1 and an S2 peak that forms an event. As a last step of the reconstruction process, various parameters characterizing an identified event are calculated and stored, such as the event position or energy. XENONnT uses machine learning algorithms to reconstruct the horizontal interaction position from the S2 pattern on the top PMT array. The energy is determined with eq. (2.1) introduced in the last section.

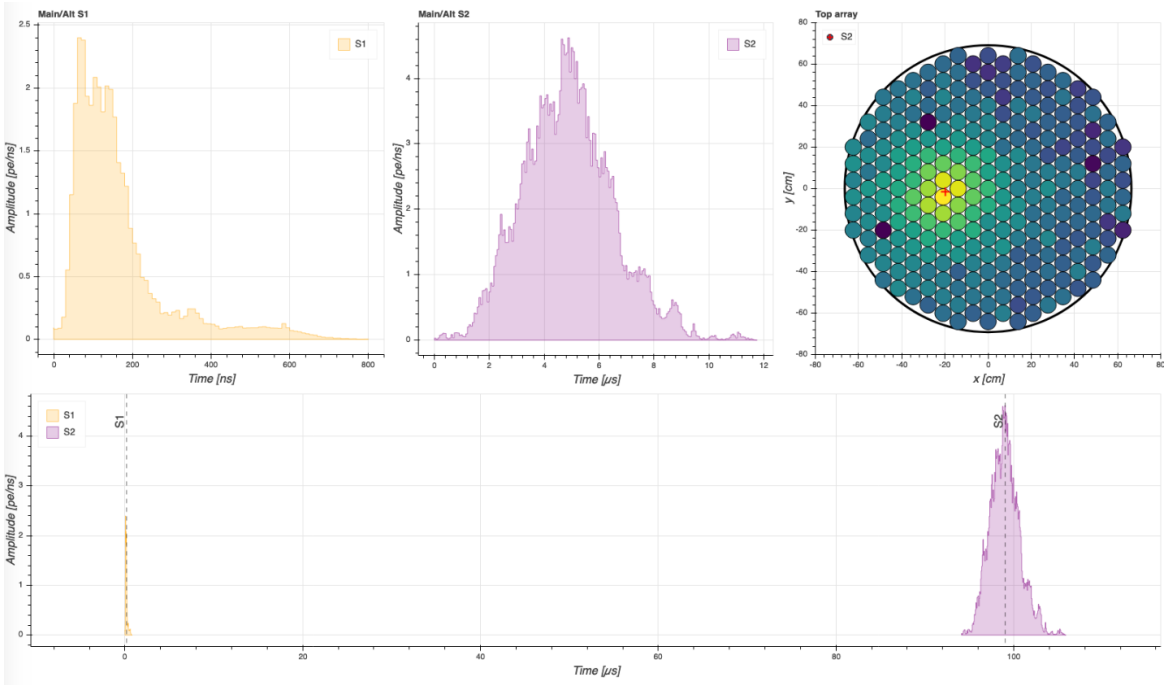

Figure 2.5: Waveform of a successfully reconstructed event containing an S1 and an S2 signal. In the upper left, the waveforms of the main S1 and S2 are shown individually. The lower panel shows the two peaks combined on a time scale of µs. The S2 PMT hit-pattern in the upper right shows the reconstructed position as red marker, whereby the color scale indicates the amount of light detected per PMT. Credit: XENON collaboration.

2.4 Calibration source ^{83m}Kr

In XENONnT, several radioactive sources are employed to calibrate the detector. The calibration source ^{83m}Kr, in the focus of chapter 3, is used for several purposes: the energy calibration, position and signal corrections, and detector stability monitoring. The metastable isomer decays in two transitions to the ground state by releasing internal conversion electrons followed by auger electrons, γ- or x-rays [54]. Figure 2.6 illustrates the branching fractions of the different decay modes. The metastable state with a half-life of 1.83 h decays to an intermediate state with a half-life of only 154 ns. The first transition releases 32.1 keV of energy and the subsequent transition 9.4 keV. The wide application of the source in XENONnT is based on several advantageous properties of the source. The half-life of 1.83 h is short enough that the source does not contaminate the detector for a longer period of time, but vanishes quickly after the calibration is complete. On the other hand, the half-life is long enough for the source to be homogeneously distributed in the detector, which is required to make signal cor-

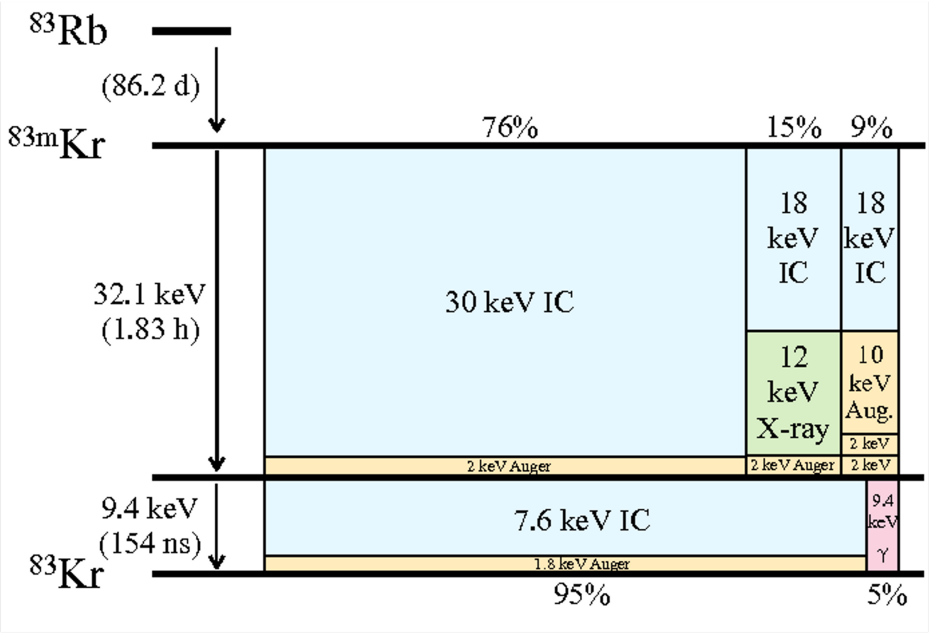

Figure 2.6: Decay scheme of ^{83m}Kr with the branching fractions of the different decay modes. The two transitions of 32.1 keV ($S1_a$) and 9.4 keV ($S1_b$) release internal conversion (IC) and Auger (Aug.) electrons, and gamma- (γ) and x-rays. Figure adapted from [54].

rections throughout the detector. The source is injected into the XENONnT TPC through an emanation chamber connected to the gaseous purification system. The chamber contains the parent isotope ^{83}Rb, which has a half-life of 86.2 d and produces ^{83m}Kr via electron capture. While ^{83m}Kr emanates as gas and mixes with xenon, ^{83}Rb remains contained in the chamber [55].
In liquid xenon, the two subsequent decays of ^{83m}Kr produce two mono-energetic energy depositions. However, due to the short-lived intermediate state (154 ns), it is difficult to measure distinct S1 and S2 peaks for each transition. For most reconstructed ^{83m}Kr events in XENONnT, the peaks cannot be separated but are observed as one merged S1 and one merged S2 peak, corresponding to an energy of 41.5 keV [56]. For decays more than about 350 ns apart, the two S1 peaks can be separated and are stored as an event with a main and an alternate S1. The S2 signals have a larger width due to the diffusion of the drift electrons and extraction process. Therefore, they cannot be separated and are always stored as one merged main S2. The positions of the two interactions occur within $\mathcal{O}(10\ \mu m)$ ([54]), whereas the position reconstruction uncertainty is $\mathcal{O}(2$ cm) in XENONnT. Hence, they are not separable.

2.5 Corrections

As the detectors response to an interaction is not uniform, several corrections need to be applied to the reconstructed events. In the following, it is detailed what kind of corrections are applied in XENONnT to achieve a position and energy reconstruction that is independent of the interaction type and position.

Position

The position reconstruction is affected by the electric drift field that is not completely uniform. Mainly at the bottom of the detector and high radii, boundary effects introduce a horizontal component on top of the vertical component of the drift field [4]. The electrons are drifted inwards such that the reconstructed positions are biased to smaller radii. To correct the bias, the homogeneous distribution of ^{83m}Kr is used. A correction map in $r = \sqrt{x^2 + y^2}$ and z is derived by requiring that the reconstructed event coordinates of ^{83m}Kr are distributed homogeneously within the active volume of the detector.

Energy

The energy is reconstructed from the weighted sum of the peak areas of S1 and S2. In the following, the measured peak areas in PE are denoted in italics by $S1$ and $S2$, while S1 and S2 refer to the signals themselves. Because of the linear anti-correlation of $S1$ and $S2$, the reconstructed energy is independent of the electric drift field [57]. A locally higher drift field enhances the ionization and $S2$ but diminishes at the same time the recombination and $S1$, and vice versa. Hence, the total energy is conserved. For this reason, $S1$ and $S2$ are by default not corrected for their drift field dependence. However, there are multiple position-dependent measurement efficiencies that affect $S1$ and $S2$. These need to be corrected. The energy is then determined with the corrected signal areas $cS1$ and $cS2$:

$$E = W \left(\frac{cS1}{g_1} + \frac{cS2}{g_2} \right). \tag{2.2}$$

S1

Besides the non-uniform drift field, $S1$ is influenced by PMT-related efficiencies, and the light collection efficiency inside the detector, which is governed by the detector's geometry and used materials. The dependence can be expressed in terms of the light

yield, that is defined as the amount of measured photoelectrons $S1$ divided by the energy E of an interaction and is given as follows [49]:

$$LY = \frac{S1}{E} = PY(E, F(r,\phi,z)) \cdot \epsilon_{QE} \cdot \epsilon_{CE} \cdot \epsilon_{LCE}(r,\phi,z) \tag{2.3}$$

PY is the photon yield, i.e. the number of scintillation photons per deposited energy E. It depends not only on the local strength of drift field $F(r,\phi,z)$ but also on the interaction type and energy. The quantum efficiency ϵ_{QE} indicates the probability of one PE being emitted at the photocathode of a PMT, and ϵ_{CE} accounts for the collection efficiency of the first dynode within a PMT. Both ϵ_{QE} and ϵ_{CE} are here the average efficiencies of all PMTs together. The light collection efficiency ϵ_{LCE} is defined as the number of photons reaching a PMT per emitted scintillation photon. This is the second position-dependent factor: reflection on the walls and the liquid-gas interface leads to less S1 light being detected by the top PMT array compared to the bottom array. Attenuation in the liquid and absorption on TPC materials decrease the total collection of S1 light.
This effect is corrected with a light collection efficiency map that is derived with the merged mono-energetic signal of ^{83m}Kr [4]. Thereby, the electric field dependence has to be separated from geometrical effects in order to achieve a purely geometrical correction factor. Figure 2.7a shows a 2D geometric correction map for S1. With the map, the local $S1$ is normalized to the mean $S1{=}\langle S1\rangle$ of all events inside the TPC with the correction factors $L_c(r,z,\varphi)$:

$$L_c(r,z,\varphi) = \frac{LY(\epsilon_{LCE}(r,\phi,z))}{\langle LY\rangle} = \frac{S1(\epsilon_{LCE}(r,\phi,z))}{\langle S1\rangle}, \tag{2.4}$$

where $\langle LY\rangle$ is the mean light yield. The corrected signal $cS1$ is is then given by:

$$cS1 = \frac{S1}{L_c(r,z,\varphi)}. \tag{2.5}$$

S2

For the S2 signal, two corrections are applied, one for the horizontal (x,y) dependence and one for the vertical dependence (z) [4]. The horizontal dependence originates from light collection efficiency $\epsilon_{LCE}(x,y)$, the extraction efficiency ϵ_{ext}, and the gas gain $G(x,y)$. The efficiency $\epsilon_{LCE}(x,y)$ is defined as in sec. 2.5 but is only horizontally dependent because for S2, all scintillation light is produced in the gas layer at the top of the TPC. The extraction efficiency ϵ_{ext} indicates the probability for a drift electron to

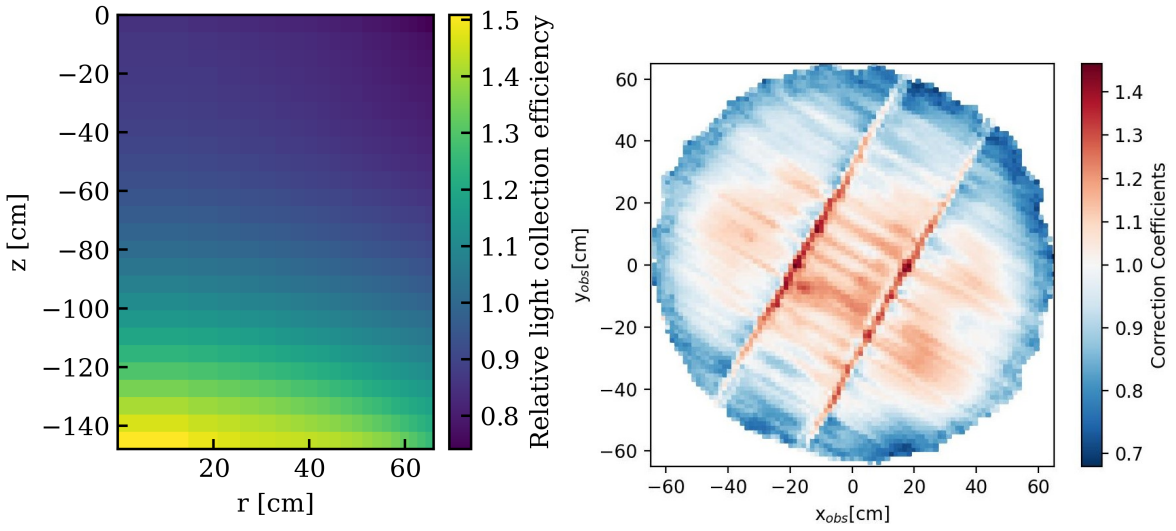

Figure 2.7: a) Geometric correction map for the light collection efficiency of S1 in r and z. b) Geometric correction map for the horizontal dependencies of S2 in x and y. The two visible lines result from a locally higher electric field due to two wires installed to prevent the gate electrode from sagging. The color scale in both maps indicates the correction factors. Figure b) from [58].

be extracted at the liquid-gas interface. The gas gain $G(x, y)$ is defined as the number of produced photoelectrons per electron that is extracted into the gas phase. $G(x, y)$ and ϵ_{ext} vary due to inhomogeneities of the extraction field and a tilted liquid level. Similarly to the S1 correction, a correction map of the horizontal (x, y) dependency of $S2$ is derived with ^{83m}Kr, shown in fig. 2.7b. The correction factors normalize the horizontal variation to the mean response of the detector [59]:

$$g_c(x, y) = \frac{G(x, y) \cdot \epsilon_{LCE}(x, y) \cdot \epsilon_{ext}(x, y)}{\langle G \cdot \epsilon_{LCE} \cdot \epsilon_{ext} \rangle}. \tag{2.6}$$

The vertical (z) dependence is due to the absorption of the drift electrons by electronegative impurities. The greater the depth z, or the longer the drift time t of an electron, the likelier it is absorbed, resulting in a smaller $S2$. This attenuation can be described by an exponential decay law with a characteristic electron lifetime τ:

$$S2 = S2_0(F(x, y, z)) \cdot \exp\left(-\frac{t}{\tau}\right), \tag{2.7}$$

where $S2_0$ is the initial charge signal and the horizontal dependence is neglected for a moment. The electron lifetime is measured with the two sources ^{83m}Kr and ^{222}Rn. The correction is then given by the inverse of eq. (2.7). Due to the constant removal

of impurities in XENONnT, electron lifetimes above 10 ms are achieved, which is significantly larger than the maximum drift time of 2.2 ms [60].
For the horizontal and vertical correction, the drift field dependence of $S2_0$ needs to be factored out. Furthermore, the two corrections cannot be decoupled. To obtain one correction, it has to be assumed that the other correction is already done. This problem can be solved by iterating the corrections several times until they converge. Finally, all parameters of $S2$ together yield:

$$S2 = S2_0(F(x,y,z)) \cdot \epsilon_{LCE}(x,y) \cdot \epsilon_{ext}(x,y) \cdot G(x,y) \cdot \exp\left(-\frac{t}{\tau}\right). \tag{2.8}$$

Both corrections combined give then the corrected signal $cS2$:

$$cS2 = \frac{S2}{g_c(x,y) \cdot \exp\left(-\frac{t}{\tau}\right)}. \tag{2.9}$$

In conclusion, the corrections applied to the S1 and S2 signal remove their position-dependencies, with the exception of the drift field dependence. As explained, the reconstructed energy, that is used for signal searches, is independent of the drift field. However, this is only true, if the field dependence of $S1$ and $S2$ is factored out of the $S1$ and $S2$ corrections. Otherwise, the corrections are biased by the field dependence of a certain calibration source and the anti-correlation is no longer given. Therefore, the electric drift field inside the TPC has to be known to correct the possible impact of a non-uniform field.

Chapter 3

Characterization of the electric drift field

The application of the electric drift field enables the measurement of ionization electrons by suppressing the recombination of electron-ion pairs and drifting the free electrons to the liquid-gas interface. However, its non-uniformity affects the position measurement as well as the amount of scintillation and ionization produced in an interaction. Section 2.5 showed that these effects need to be taken into account in the corrections of reconstructed signals. In order to remove field effects in the corrections, the actual electric field in the detector needs to be simulated or reconstructed from data. A simulated map can offer a high resolution and is not limited by statistics of calibration data. However, it needs to be validated with such data. Therefore, this work reconstructs the electric drift field with ^{83m}Kr calibration data.

The chapter is organized as follows: The configuration of the electric field in XENONnT is detailed in section 3.1. Section 3.2 presents the field simulations of XENONnT. Section 3.3 covers the data-driven reconstruction of the drift field. Section 3.4 investigates the impact of the non-uniformity of the drift field. The last section 3.5 discusses the obtained results and the potential of the data-driven approach for the field reconstruction.

3.1 Electric field configuration in XENONnT

In XENONnT, the electric fields are generated by five electrodes and two sets of concentric field-shaping rings [4]. Figure 3.1 shows the different contributing parts and their positions in the TPC. Table 3.1 summarizes the voltages that were applied during

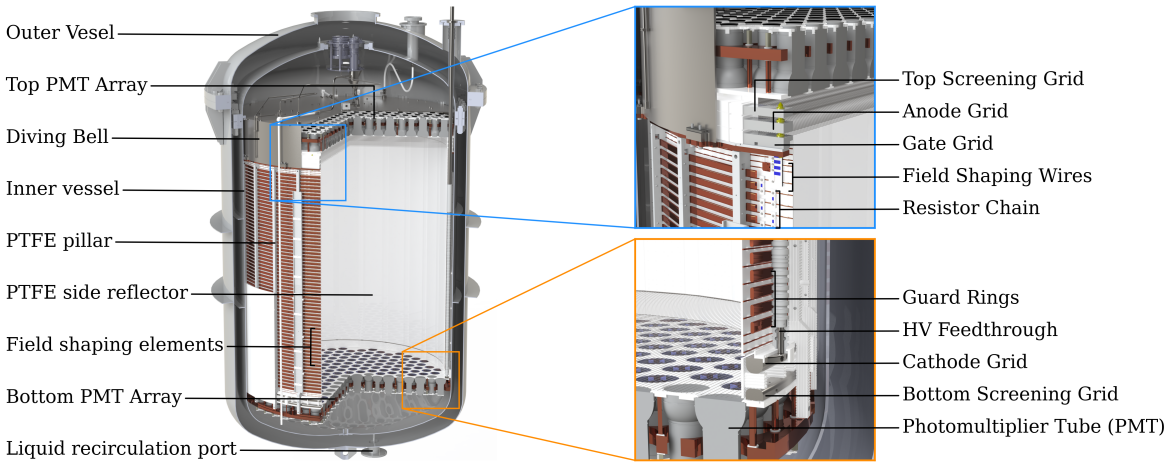

Figure 3.1: Sketch of the TPC with zoom into the top and bottom region, where the five electrodes are situated. Image credit: XENON collaboration.

Electrode	Potential [kV]
Top screen	- 0.9
Anode	+ 4.9
Gate	+ 0.3
Top field-shaping wire	+ 0.65
Cathode and bottom screen	- 2.75

Table 3.1: Configuration of the electric field during the first science run of XENONnT.

the first science run of XENONnT.
All five electrodes are made of parallel stainless-steel wires. Two of them are installed slightly above the anode and below the cathode to screen the two PMT arrays from from high electric fields. The extraction field of 2.9 keV/cm across the liquid-gas interface is generated by the anode and the gate grid. The wires of these two grids have a pitch of 5 mm. In addition, the anode and the gate are supported by four and two perpendicular wires, respectively, to minimize the sagging of the grid.
The drift field is generated by the negatively biased cathode, the positively biased gate grid and the field cage. With 23 V/cm on average, it is about four times lower than in XENON1T due to a short-circuit between the cathode the bottom screen, limiting the voltage that can be applied. The wires of the cathode have a pitch of 7.5 mm. The field cage consists of two sets of alternating field-shaping wires and guard rings, surrounding the drift region of the TPC to make the drift field as uniform as possible. The rings are connected by two redundant chains of resistors. The bottom ring is connected to

the cathode, while the top ring is biased independently at 0.65 kV.
It was observed in XENON1T that free electrons accumulated on the PTFE side walls of the TPC [61]. This induced a contribution to the drift field that increased over time. As this charge-up effect was also expected for XENONnT, avoidance measures were put in place: the field shaping wires are installed in direct contact with the PTFE walls, and 360 holes are placed in the wall panels such that the accumulated charge can more easily be collected by the wires. For the drift field simulations, the charge-up effect needs to be taken into account and yields an effective drift field. The data-driven approach directly reconstructs the effective drift field present in the detector.

3.2 Simulation of the electric drift field

In XENONnT the COMSOL Multiphysics software is used to simulate the electric drift field [62]. COMSOL allows to simulate the electric field for a given geometry and configuration of electrodes in two and three dimensions. Using the approximately axisymmetric geometry of the TPC, the simulation for XENONnT is done in 2D, in the radius r and the depth z [61]. To make the simulation faster, the field of each contributing electrode is simulated individually. By the superposition principle, the sum of the individual parts then yields the total drift field.

To include the charge-up effect, an individual map of the electric field induced by the accumulated charge can be produced with COMSOL. However, the charge distribution at the PTFE walls is unknown. To find the correct charge distribution, different configurations are simulated and matched against the radial distribution of ^{83m}Kr events that is only dependent on the drift field. The charge distribution is modeled as a linear gradient on top of a constant charge. The total drift field is then simulated with around 1000 different configurations of the charge distribution. For each simulated total field, the radial event distribution is simulated by propagating electrons along the field lines. The resulting distribution is compared to the measured distribution of ^{83m}Kr events. The best matching values for the charge distribution are -0.5 μC/m^2 at the top and -0.1 μC/m^2 at the bottom of the TPC, with a linear gradient in between.

Figure 3.2 shows the resulting simulated maps with and without charge-up effect. There is a clearly visible difference between the two maps. The charge-up effect diminishes the field at the walls and the bottom, whereas it enhances the field towards the top. The electric field map that was derived from simulations and ^{83m}Kr drift electron paths can be validated further by a field reconstruction based on ^{83m}Kr S1 yields.

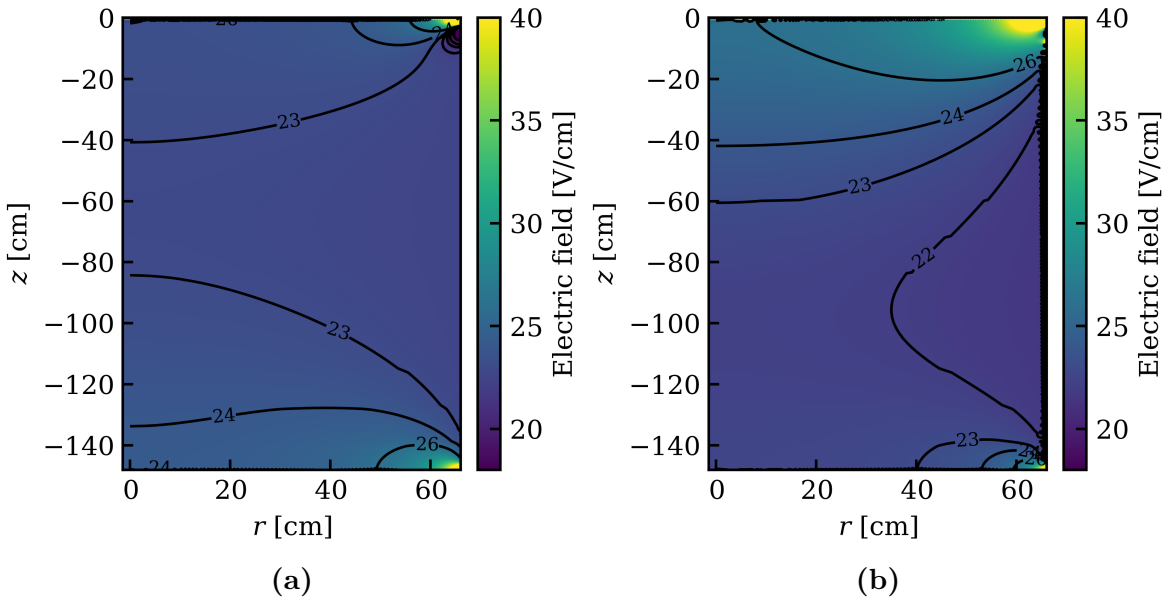

Figure 3.2: Simulated map of the drift field a) without the charge-up effect b) including the charge-up effect. The black contour lines connect positions of equal field strength.

3.3 Data-driven reconstruction with ^{83m}Kr

In the following, the electric drift field is reconstructed with ^{83m}Kr calibration data. The electric field strength is thereby mapped in two and three dimensions for the entire drift region of the TPC. Whereas the three dimensional map can evaluate the non-uniformity of the drift field across the entire TPC, the two dimensional map will be used for the comparison with the simulations. First, the data-driven reconstruction method is introduced, followed by the selection and analysis of the ^{83m}Kr data, the presentation of the resulting drift field maps and the comparison with simulated maps.

3.3.1 Electric field dependence of the light yield

To reconstruct the electric drift field across the TPC, the data-driven approach makes use of the field dependence of the light yield [54]. The light yield LY was introduced in sec. 2.5 and is defined by eq. (2.3). LY depends on the local field strength at the interaction position but also the measurement efficiencies of the detector. However, by taking the ratio of the areas of two S1 signals, $S1_a$[1] and $S1_b$ of different energies E_a and E_b, that occur at the same position, the PMT-related efficiencies ϵ_{QE} and ϵ_{CE} as well as the light collection efficiency ϵ_{LCE} cancel out:

[1]The non-italic font refers to the signals themselves, while the italic font refers to the measured peak areas of the signals.

$$\frac{S1_b}{S1_a} = \frac{PY_a(E_b, F(r,\phi,z))}{PY_b(E_a, F(r,\phi,z))} \cdot \frac{E_a}{E_b}. \tag{3.1}$$

For two signals $S1_b$ and $S1_a$ that originate from interactions with a different field dependence, the peak area ratio $S1_b/S1_a$ is a measure that varies only with the local drift field strength $F(r,\phi,z)$. With a model describing the field dependence of the photon yields PY_a and PY_b, the ratio can then be converted into an electric field strength. Hence, with measurements of the scintillation light from two distinct interactions, the electric field can be reconstructed.

The calibration source ^{83m}Kr is well suited for this data-driven reconstruction method. As described in sec. 2.4, the two-staged decay of ^{83m}Kr delivers events with two mono-energetic S1 signals at 32.1 and 9.4 keV that yield $S1_a$ and $S1_b$, respectively, at the same interaction position. The homogeneous distribution of the events further allows to reconstruct a field map of the entire detector. And due to the practical employment and wide use in XENONnT, calibrations with ^{83m}K are conducted regularly such that a significant amount of data is available.

Yield-to-field models

Different models are available for converting the photon yield to the electric field strength. One option is the semi-empirical model provided by the simulation software Noble Element Simulation Technique (NEST) [63]. NEST can be used to simulate the energy deposition process in liquid noble element detectors, from the energy deposition up to the Pulse shape in PMTs [64]. It provides models for different interaction types, also one specifically for ^{83m}Kr. Nevertheless, the tool is not used for the reconstruction of the drift field because a more recent model is available that is based on direct measurements of the dependence between the light yield ratio of ^{83m}Kr and the field strength.

The empirical model was obtained with a dual-phase xenon TPC called HeXe at the Max Planck Institute for Nuclear Physics [65]. HeXe is a cylindrical TPC with a drift volume of 5.6 cm in diameter and 5 cm in height and was developed for research and development purposes. It is equipped with two 2-inch PMTs. The electric extraction and drift fields are applied with a field cage and electrode meshes, whose design is optimized for a uniform drift field. To obtain a model for the relation between $S1_a/S1_b$ and the drift field strength F, the signals from ^{83m}Kr decays were measured for different applied voltages. Note that this model uses, by convention, the inverted ratio of eq. (3.1), such that the larger $S1_a$ (32.1 keV) is divided by the smaller $S1_b$ (9.4 keV). The results and the fit of the data are shown in fig. 3.3. The ratio decreases as a function

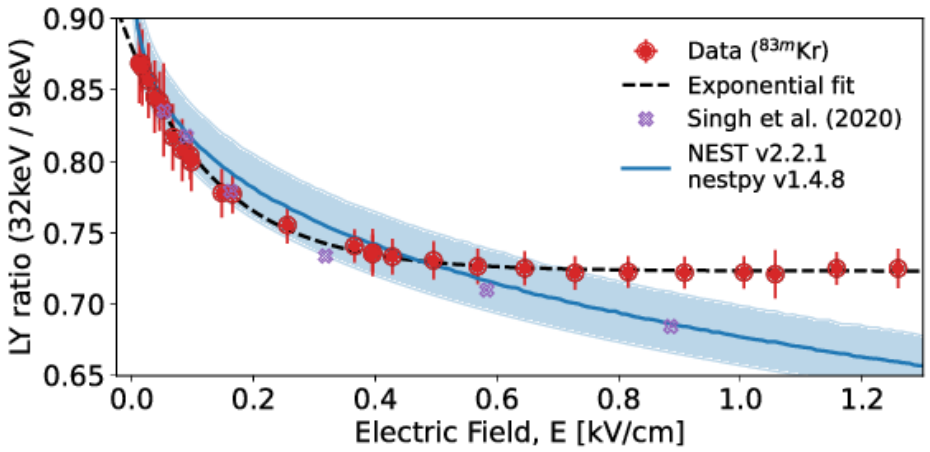

Figure 3.3: HeXe model for the light yield ratio of ^{83m}Kr as a function of the electric drift field. The measurements are fitted with a phenomenological function. The model from NEST is shown in blue with a shaded area indicating the range for different delay times. Figure from [65].

of the field strength because the light yield of the first decay decreases faster than the light yield of the second. The measurements cover drift fields down to 7.5 V/cm and thus the relevant range for XENONnT, that has a mean drift field of 23V/cm. For the fit, a function purely motivated by the observed phenomenology was used:

$$R(F) = \frac{LY_a(32\text{ keV})}{LY_b(9\text{ keV})} = \frac{S1_a(32\text{ keV})}{S1_b(9\text{ keV})} \cdot \frac{9\text{ keV}}{32\text{ keV}} = b_1 \cdot e^{-b_2 \cdot F} + b_3, \tag{3.2}$$

where b_1, b_2 and b_3 are the fit parameters. The fit describes the data well and agrees at lower electric field with the model from NEST [66].

Delay time dependence of the ratio $S1_b/S1_a$

As both S1 signals from ^{83m}Kr originate from subsequent decays of the same nucleus, they have to be separated far enough in time to be registered as two signals as mentioned in sec. 2.4. This capability depends on the physical delay of the two decays as well as on the signal reconstruction in the detector. Moreover, the timescale of the recombination physics determining the signal yields induces a delay-time dependence of the second $S1$ that affects the measured ratio $S1_b/S1_a$. As observed here [67] and here [68], the photon yield of the second decay of 9.4 keV depends on the time between the first and the second decay, denoted as delay time in the following. If the delay time is short, the cloud of electrons left over from the first decay enhances the recombination of electron-ion pairs in the second decay, resulting in an increased photon yield.
The delay time dependence can introduce a systematic bias for the drift field recon-

struction in two ways. First, if the delay times of the events are not distributed equally across the detector, the ratio $S1_b/S1_a$ does not only vary with the drift field strength but also with the delay time distribution. Therefore, the delay time needs to be considered when selecting events for this analysis, as discussed in sec. 3.3.2. Second, the use of the HeXe model for this analysis can introduce a bias if the delay time distribution of the events used for the HeXe model is not the same as in XENONnT. To minimize the delay time dependence as much as possible, the HeXe model only selected events with a delay time above 300 ns, even though the detector could resolve two distinct S1 peaks for delay times above 50 ns [65]. However, XENONnT can only resolve distinct S1s with time differences above around 350 ns. This problem will be addressed in sec. 3.3.3.

3.3.2 Data selection

The goal of the data selection is to select as many ^{83m}Kr events as possible with two reconstructed S1 peaks, one from the first decay of 32.1 keV and one from the second decay of 9.4 keV. During the first science run of XENONnT, calibrations with ^{83m}Kr were conducted approximately every two weeks. The data used for this analysis was collected between May and November 2021 and includes in total 17.5 (live) days of calibration data. Livetime as opposed to real time is corrected for busy periods of the data acquisition system.

Figure 3.4 shows all events of the dataset that contain a main S1 ($S1_a$) and an alternate S1 ($S1_b$). The peak areas of the S1 signals are thereby not corrected for the varying light collection efficiency in the TPC. The cluster in the middle with $S1_b \approx 100$ PE corresponds to the ^{83m}Kr events with two resolved S1 peaks. These are the events that are selected to perform the reconstruction of the electric drift field. The events in the bottom cluster are merged S1 peaks from ^{83m}Kr with a small $S1_b$ originating from noise. The smeared-out cluster at the top consists of pile up events from multiple ^{83m}Kr decays.

The specific parameters to select the ^{83m}Kr events with two S1 peaks and one S2 peak are adopted from the XENON collaboration and are summarized in tab. A.1 in the appendix [56]. As the different event populations in fig. 3.4 overlap to some extent, the events are not selected directly in the space of $S1_a$ and $S1_b$, but a variety of other event parameters are used. Three selection cuts are applied to remove events that contain an $S1_b$ signal that is merged with an afterpulse signal. An afterpulse is generated inside the PMTs by the ionization of residual gas atoms or molecules from an initial photoelectron. The ions then hit the photocathode and eject a delayed photoelectron, with the delay time being characteristic for the ion and the PMT type. Figure 3.5 shows

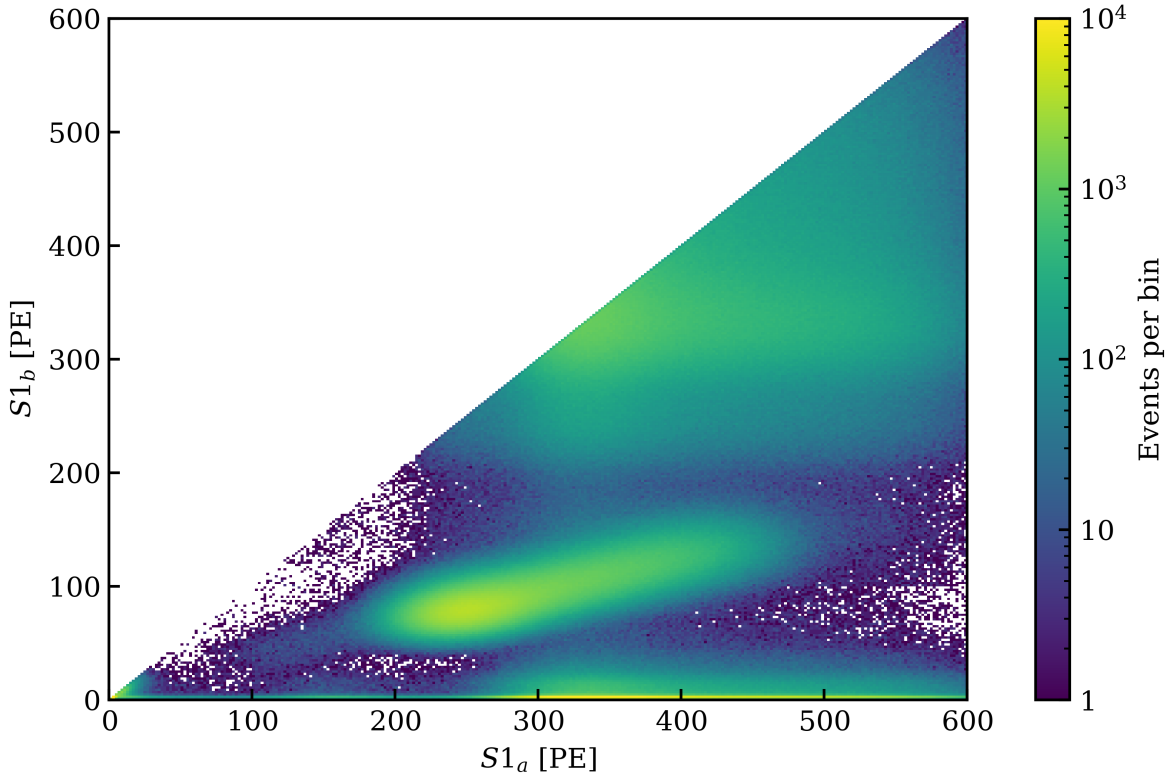

Figure 3.4: Histogram of all events recorded during ^{83m}Kr calibrations, plotted in the space of the uncorrected $S1_a$ and $S1_b$ with a binning of (2×2) PE^2. The main S1 is denoted as $S1_a$ and the smaller alternate S1 as $S1_b$.

one of the selection cuts that removes events containing an $S1_b$ peak merged with a He^+ afterpulse. It is important to remove those events because the afterpulse increases $S1_b$ and thus would affect the electric field reconstruction that relies on $S1_b/S1_a$.

Another quantity that could affect the field reconstruction is the delay time of the events as discussed in sec. 3.3.1. Figure 3.6 shows that the delay time distribution of the events is not the same for all slices of the detector along the vertical axis z. For short delay times below 500 ns it becomes more difficult for the peak splitting algorithm to reconstruct the two S1 peaks individually, especially at the top of the TPC, where the light collection efficiency is lower. To avoid differing delay time distributions from slice to slice, which would introduce a position dependent bias, only events are selected with a delay time larger than 500 ns. For the range above 500 ns, fig. 3.6 demonstrates that the delay times are distributed equally. Note that this cut is specified for this analysis and deviates from the default selection of XENONnT for ^{83m}Kr events with two S1 peaks. The default cut for the upper limit of the delay time is adopted. The cut removes events with a delay time larger than 2000 ns, where more afterpulses are

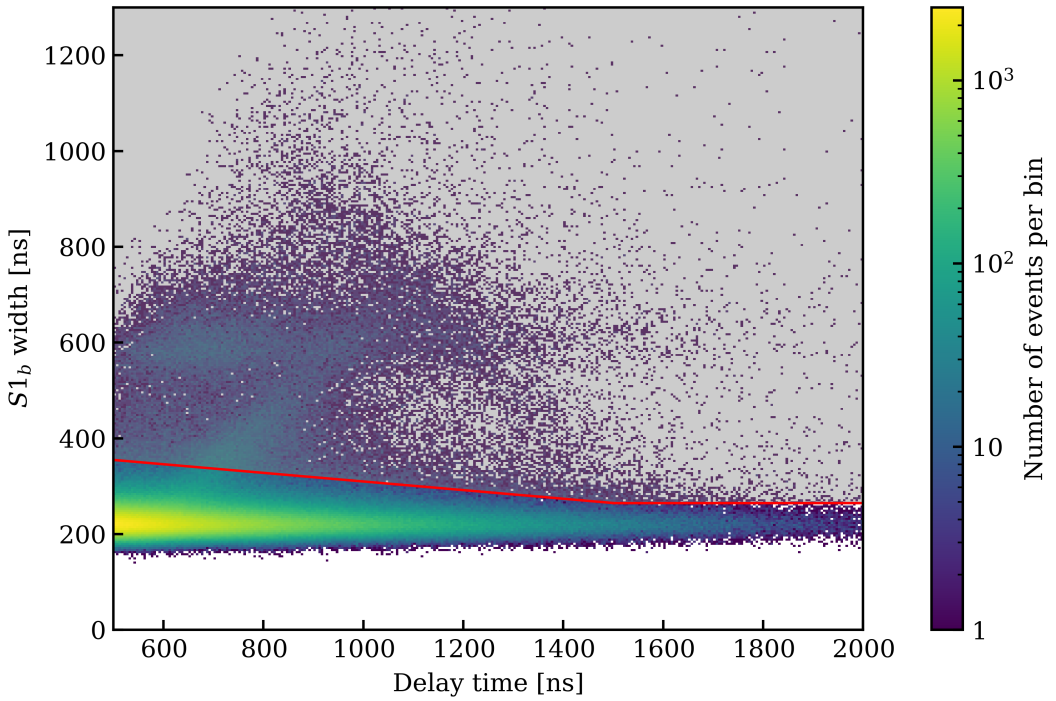

Figure 3.5: Selection cut to remove events where the $S1_b$ peak is merged with an afterpulse. The events above the red line are removed. The delay time is defined as the observed time between the $S1_b$ and $S1_a$ signal. The histogram has a binning of (4.3×6.7) ns^2.

observed.

The remaining 3.4×10^6 events after all selection cuts are depicted in fig. 3.7a. As shown in fig. 3.7b, the selected events are not distributed completely homogeneously across the TPC. The inhomogeneity is present because part of the data was collected while the calibration source ^{83m}Kr was injected into the detector and had not yet distributed throughout the detector. This increases the amount of available statistics, while the small inhomogeneity is not an issue for this analysis. The selected events show a good agreement with the expected half-life of ^{83m}Kr. To extract the half-life, a χ^2-fit is performed on the histogram of the delay times with an exponential decay law, shown in fig. 3.8. The fit-region is restricted to delay times between 800 and 1500 ns, because the reconstruction efficiency is not only decreasing for shorter but also for longer delay times. It becomes increasingly likely for longer delay times, that the $S1_b$ overlaps with an S2 from another event and cannot be reconstructed. The best-fit half-life is relatively close to the literature value of 154 ns for the intermediate state of ^{83m}Kr. Some deviation is expected since the time of an event is defined in the middle of the peak and not at the beginning, which limits the time resolution.

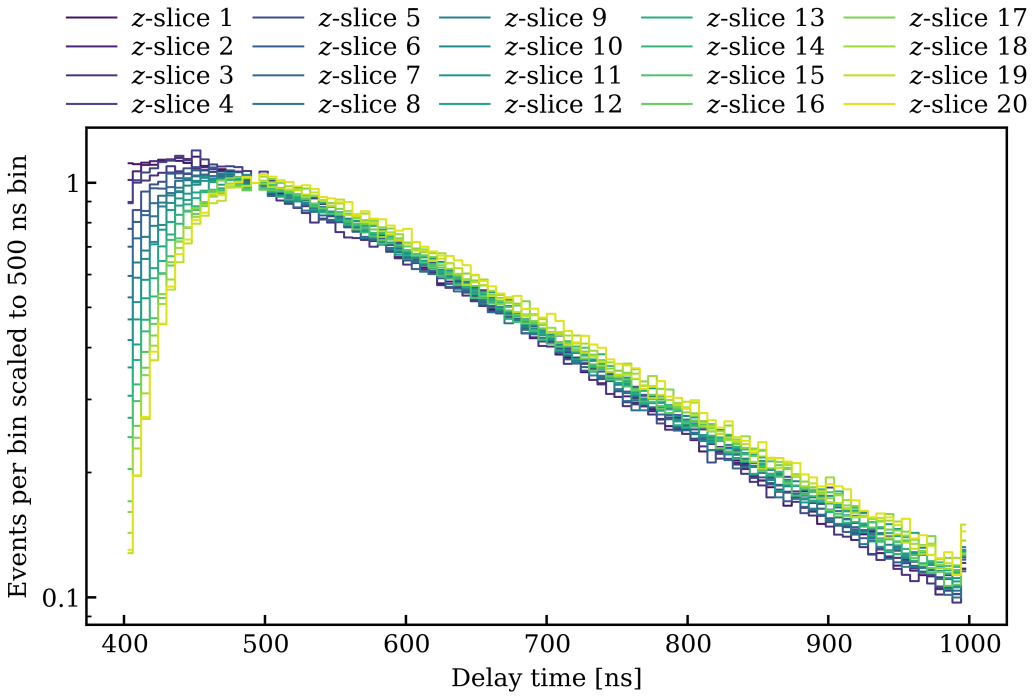

Figure 3.6: Histograms of the delay time between $S1_b$ and $S1_a$ for 7.4 cm thick vertical slices of the TPC drift region. Slice 1 is the most bottom and slice 20 the most top slice, respectively. The bin entries are normalized by the bin entry at 500 ns.

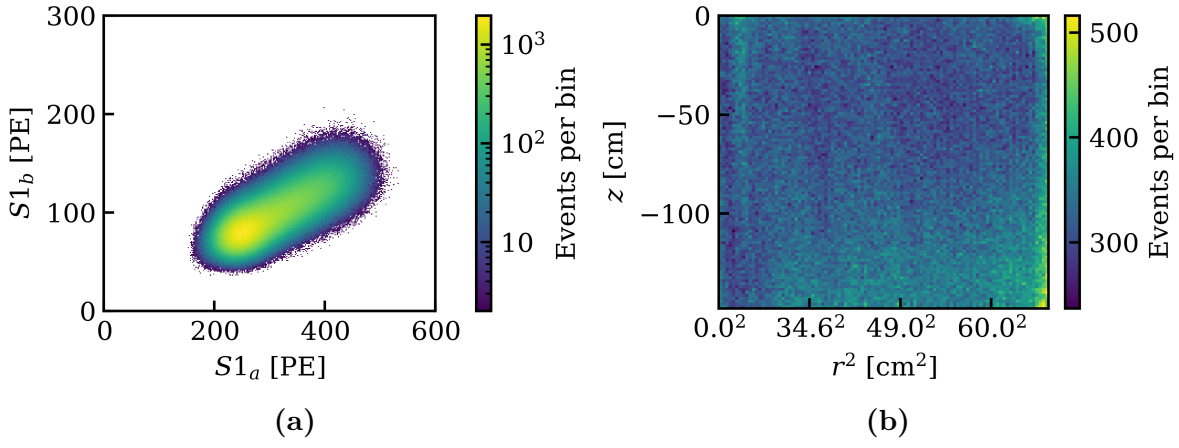

Figure 3.7: a) Histogram of the selected event for the reconstruction of the electric field, plotted in the space of the uncorrected $S1_a$ and $S1_b$ area with a binning of (2×1) PE^2. b) Histogram of the spatial distribution of the selected events in bins of equal volume in z and r^2 with a binning of (44×1.5) cm^3.

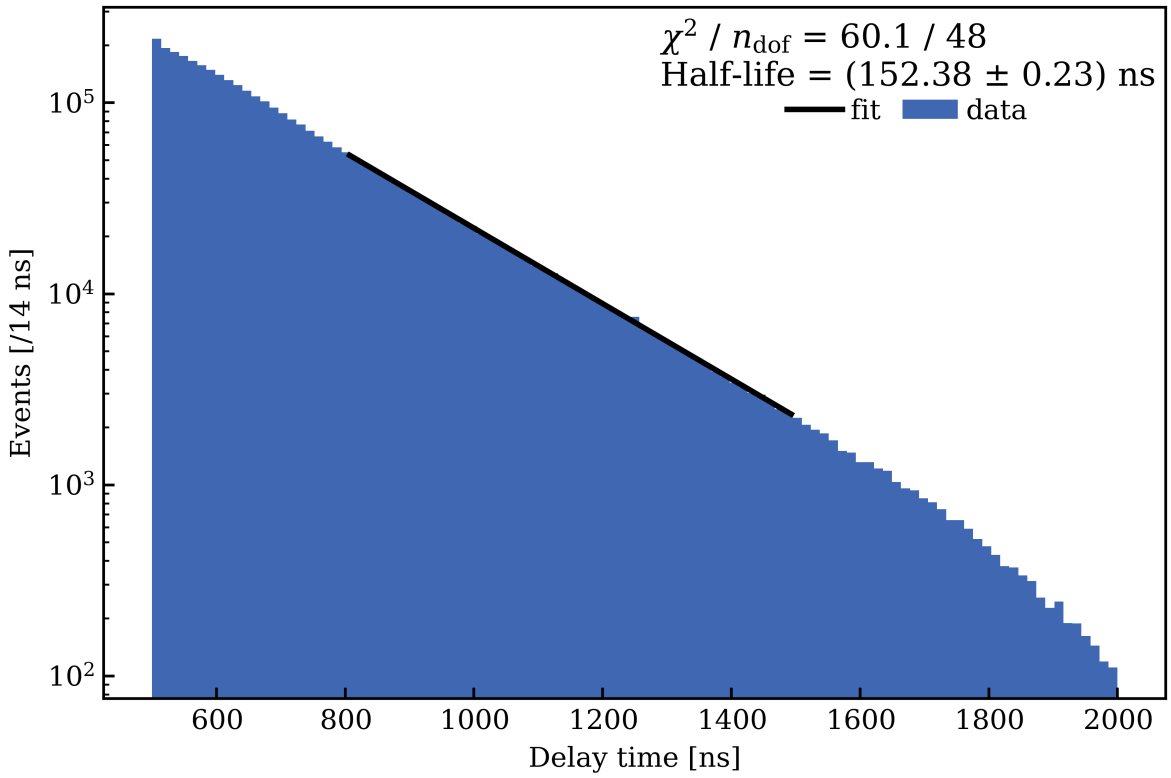

Figure 3.8: Histogram showing the delay time distribution of all selected events. The black line represents the best fit from a χ^2-fit with an exponential function for delay times between 800 and 1500 ns.

3.3.3 Data analysis

The drift field is reconstructed with the selected data in two main steps, following the approach outlined in sec. 3.3.1. The first step is to make a map of the peak area ratio $S1_b/S1_a$ of all ^{83m}Kr events in 2D and 3D. The second step consists of converting the mapped ratios into an electric field strength using the HeXe model presented in sec. 3.3.1.

Map of the peak area ratio $S1_b/S1_a$

To obtain a map of the ratio $S1_b/S1_a$ across the TPC in two and three dimensions, the TPC is divided into smaller segments, or bins, for which the mean ratio is extracted. The chosen number of bins is a trade-off between statistics and spatial resolution: the more events per bin, the more ^{83m}Kr events are contained for determining the mean $S1_a$ and $S1_b$, but the worse the resolution. To reconstruct the drift field as locally as possible, a number as high as possible is chosen without statistical fluctuations making trends unrecognizable. The bins are chosen to have an equal spatial volume, such that they contain approximately the same number of events. For the 2D map, the TPC is divided into 500 bins in the r- and z-direction. In the r-direction, the subdivision is made in r^2 that is proportional to the volume of each bin. For the 3D map, the TPC is divided into 540 bins in the r-, φ-, and z-direction. The bins are spaced equally in r and z, but the covered angle φ decreases with higher radii such that the bins are of equal volume. The drift region of XENONnT considered for this analysis spans in the vertical direction from z = -148 cm at the bottom to z = 0 cm at the top, and in the radial direction from r = 0 cm to r = 66 cm. The origin of the TPC coordinate system is defined by the height of the gate grid (z = 0) and the middle of the center PMT (r = 0).

In each bin, the mean $S1_a$ and $S1_b$ of all events is extracted from an unbinned maximum likelihood fit with a Gaussian function. An example of the $S1_a$ distribution in one 3D bin is presented in fig. 3.9 together with the corresponding best fit. In all bins, the distribution of the $S1_a$ and $S1_b$ is in good agreement with a Gaussian function. This implies that the chosen bin volume is small enough such that the impact of the light collection efficiency is negligible inside the bin. Otherwise, the position-dependent efficiency would skew the distribution so that it is no longer Gaussian.

Taking the ratio of the extracted mean $S1_b$ and mean $S1_a$ in each bin yields the targeted maps. Figure 3.10a shows the map in 2D, the map in 3D is not shown for this intermediate step. The map in fig. 3.10b indicates the statistical uncertainties for each bin, that are based on the propagated uncertainties from the fit of $S1_a$ and $S1_b$. The

trend in the uncertainties originates from the non-uniform distribution of the number of events in the TPC, as higher per-bin statistics lead to lower statistical uncertainties.

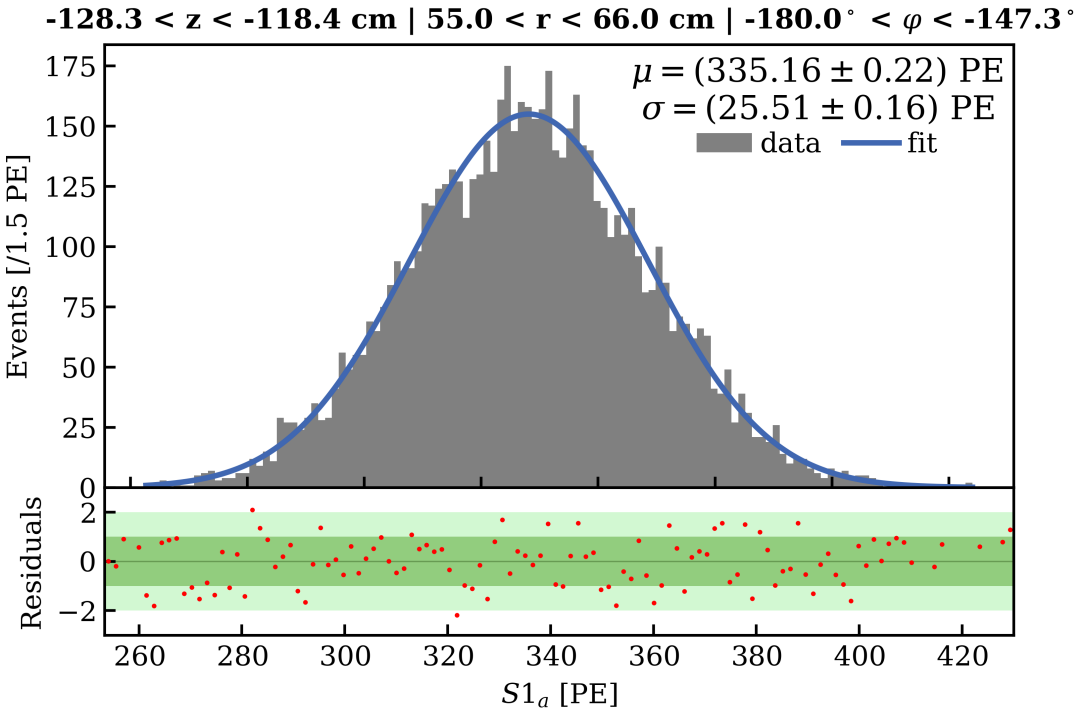

Figure 3.9: Top panel: histogram of $S1_a$ for one bin of the 3D map. The blue line represents the best-fit from an unbinned maximum likelihood fit with a Gaussian function with the mean μ and the standard deviation σ. Bottom panel: residuals of the fit normalized by the uncertainty on the number of events N_i in each bin, given by $\sqrt{N_i}$.

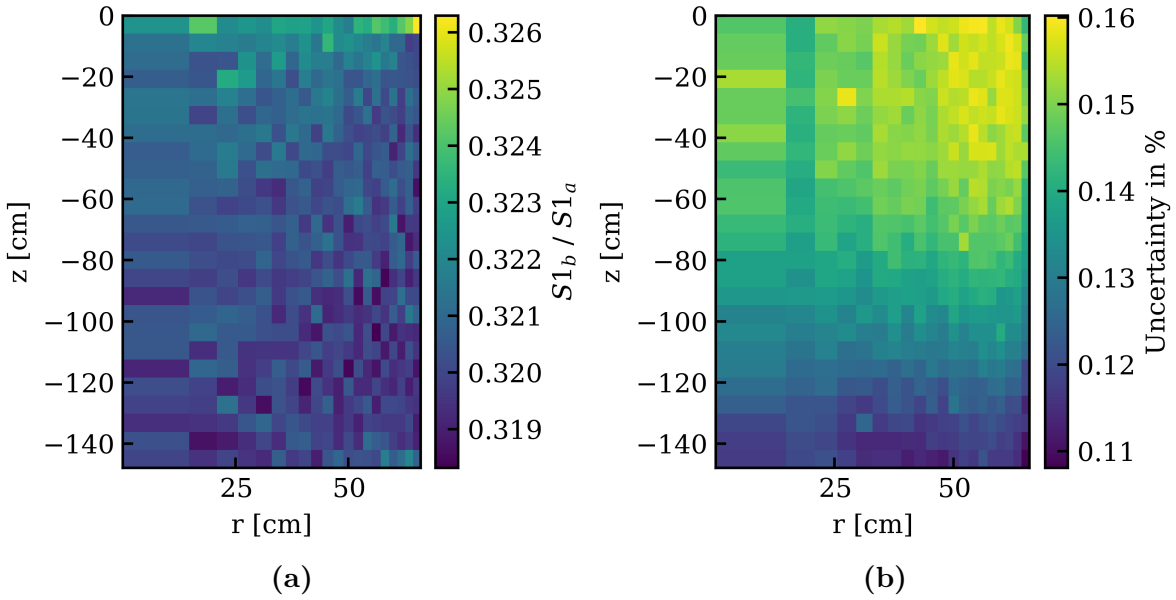

Figure 3.10: a) Map of the peak area ratio $S1_b/S1_a$ in r and z. b) Map of the relative statistical uncertainties of the peak area ratio. Both maps are divided in 20 bins in r^2 and 25 bins in z, leading to 500 bins of equal volume in total.

Conversion with the HeXe model

To convert the maps of $S1_b/S1_a$ into maps of the electric drift field, the HeXe model introduced in sec. 3.3.1 is used. However, the prediction of the model for the obtained ratio maps gives negative values for the electric field in XENONnT (see fig. 3.10a and 3.12). This is clearly unphysical. Therefore, the model cannot be applied in its original form but needs to be scaled for this analysis. The scaling of the model is supported by several arguments presented in the following [69]: one probable cause for the wrong prediction of the model is the delay time dependence of $S1_b/S1_a$ discussed in sec. 3.3.1. The HeXe model is based on events with a delay time > 300 ns, whereas for this analysis events are selected with a delay time > 500 ns and < 2000 ns. The discrepancy induces a bias to the ratio of unknown size, but if the delay time distribution of the events is the same across TPC, the bias is a constant shift. This motivates the scaling of the HeXe model with a constant factor. In addition, it is ensured that position-dependent efficiencies or differences in the signal reconstruction process of the two detectors are not the cause for the unphysical prediction, as the model is based on the ratio of two signals with the same interaction position. For these reasons, the scaling of the model with a constant factor is well-motivated.
The scaling factor is determined with the help of the simulation, which provides the only estimate of the true drift field strength in XENONnT. The model is scaled such

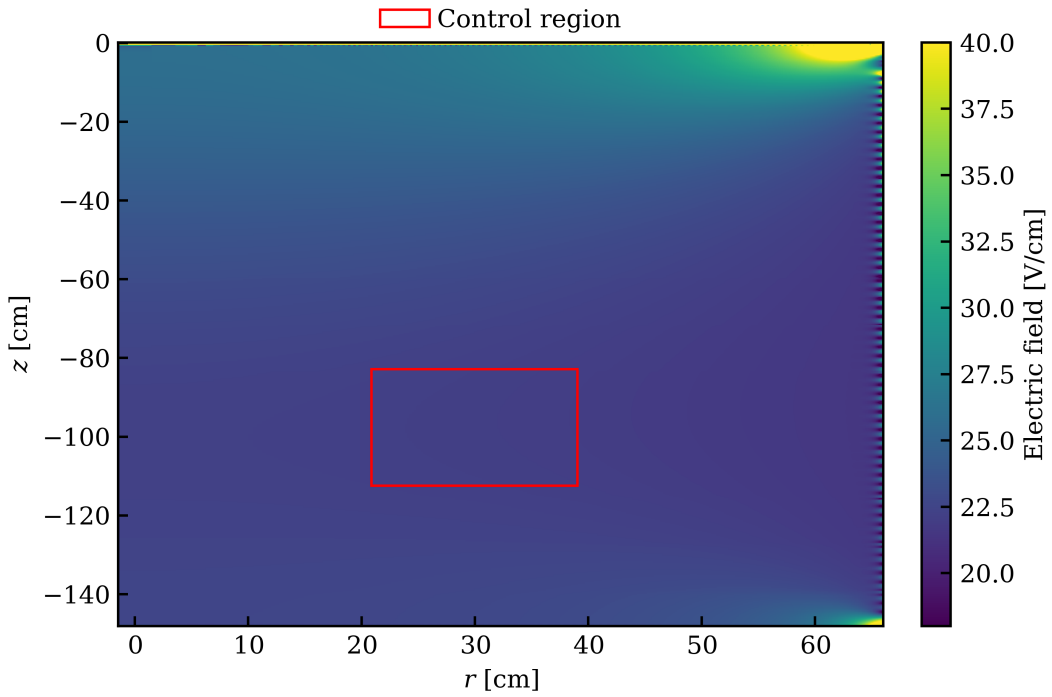

Figure 3.11: Simulated 2D drift field map including the charge-up effect. The red box indicates control region that is used to scale the HeXe model.

that the mean electric field inside a control region in the 2D data-driven map matches the mean of the same region in the simulated map, as illustrated in fig. 3.11. The control region is defined by an approximately homogeneous region in the simulated map. With the scaled model shown in 3.12, the data-driven maps of the drift field can be generated in 2D and 3D.

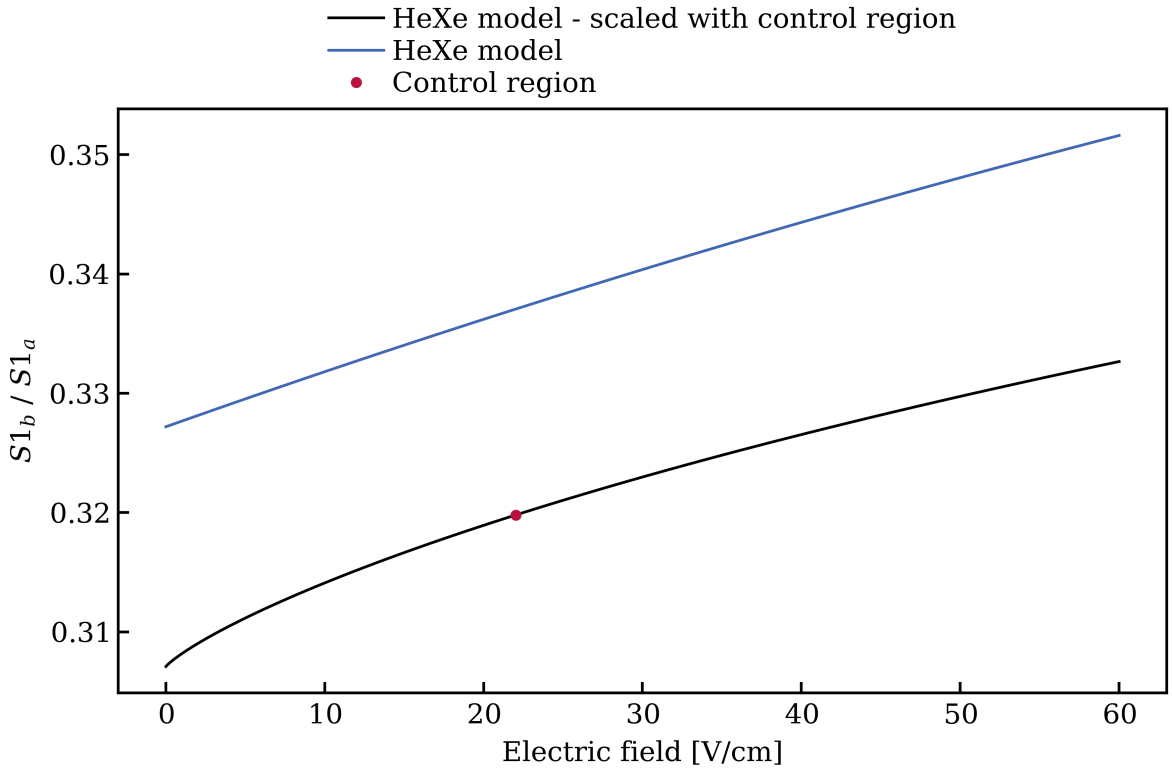

Figure 3.12: Scaled (black) and unmodified (blue) HeXe model for the relation between $S1_b/S1_a$ and the electric drift field strength for ^{83m}Kr. The red point indicates the mean electric field in the control region.

3.3.4 Electric drift field maps

The 2D map in fig. 3.13a and the 3D map in fig. 3.14 show similar trends to the one observed in the simulated maps. In the middle of the TPC, the electric field is relatively uniform. Towards the bottom and especially towards the top, the field increases. Despite the large amount of events per bin, between 5000 and 8000, and the Gaussian distributed $S1_a$ and $S1_b$, there are rather large fluctuations between neighboring bins. A statistical origin of the fluctuations is supported by the calculated statistical uncertainties of 0.8 - 1.5 V/cm, corresponding to 3.5 - 6% in relative terms. The uncertainty is derived from the statistical uncertainty on the peak area ratio. As the drift field is highly sensitive to small variations of the peak area ratio and their relation is non-linear (see eq. (3.2) or fig. 3.12), the small relative uncertainties on $S1_b/S1_a$ translate into larger relative uncertainties on the drift field. The non-linearity further leads to an asymmetric uncertainty. However, the difference is small such that only the slightly larger positive uncertainty is used. The uncertainties for the 2D map are shown in fig. 3.13b, for the 3D map they can be found in fig. A.1 in the appendix.

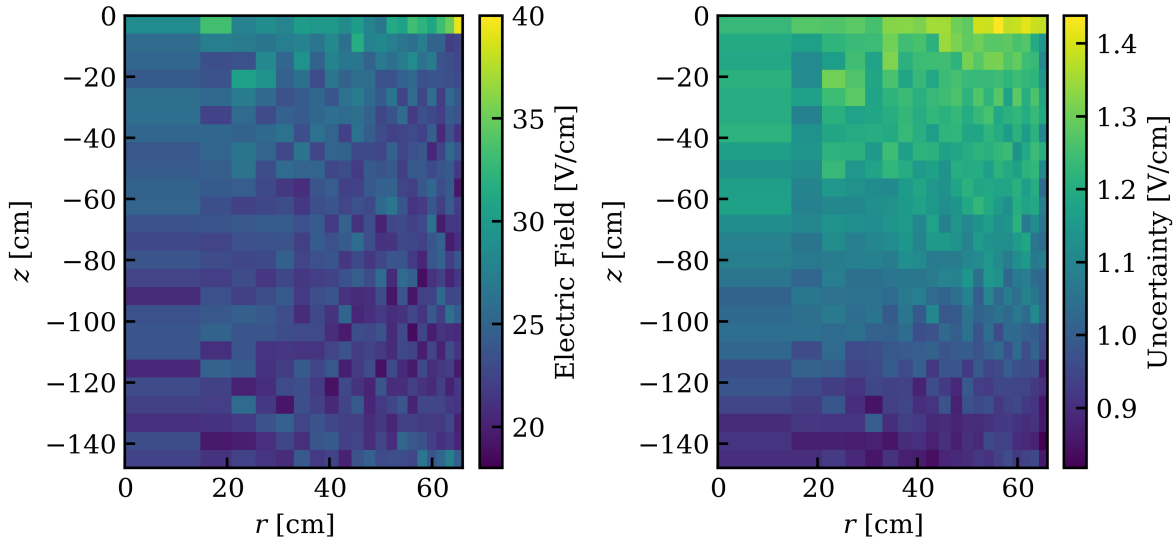

Figure 3.13: a) Data-driven map of the drift field in 2D. The color scale covers the whole range of observed field strengths. b) Map of the absolute statistical uncertainties of the reconstructed drift field strengths.

The data-driven map in 3D does not show a noticeable trend that would point to a broken axisymmetry of the electric drift field. On the other hand, the precision of the data-driven map is clearly limited by the available amount of data, such that small changes of the field strength cannot be resolved.

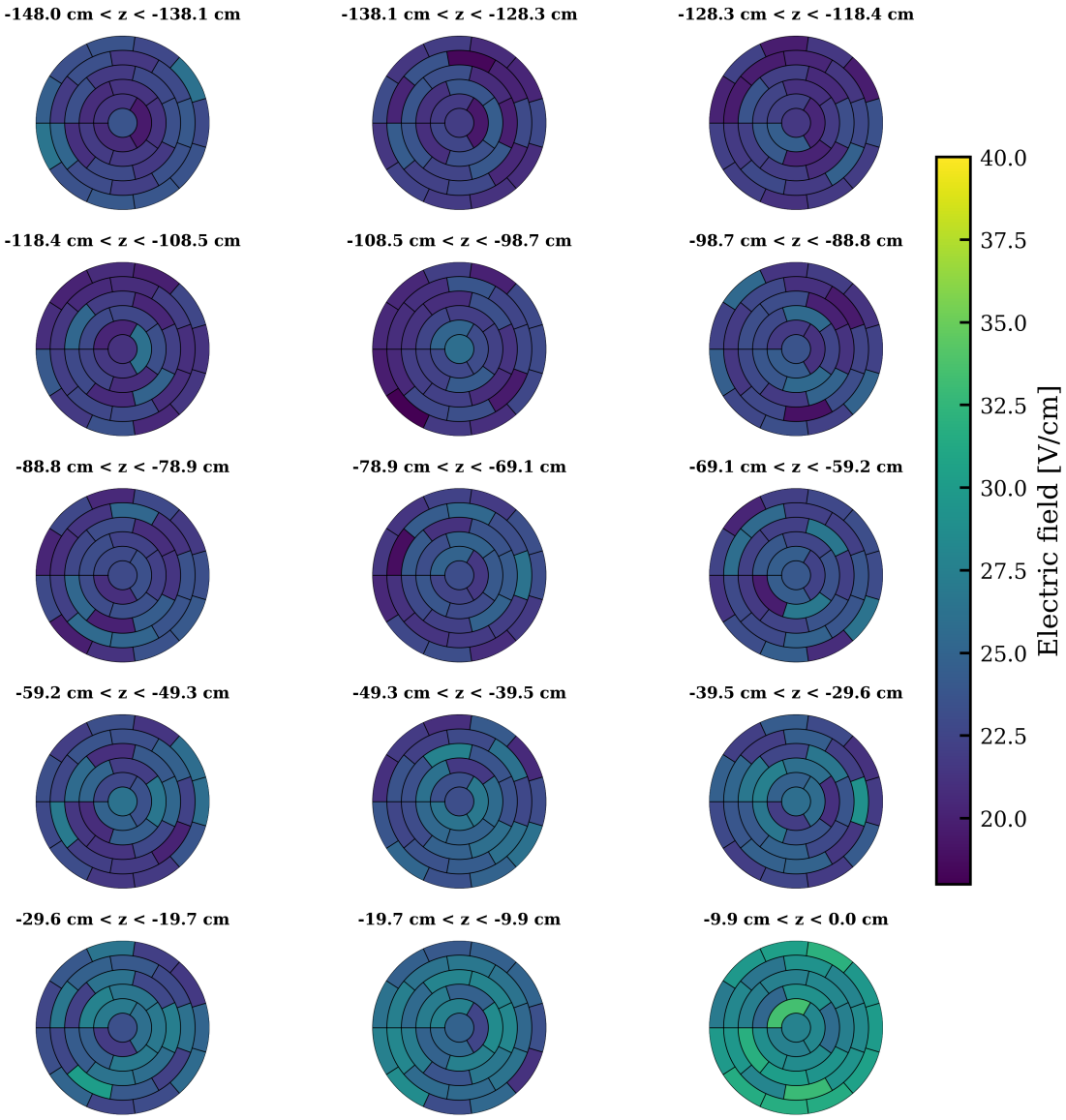

Figure 3.14: Data-driven map of the drift field in 3D consisting of 540 bins of equal volume in 15 z-slices. The color scale is fixed to the same range as the map in 2D to enable a comparison of the two maps.

3.3.5 Comparison with field simulations

For the validation of the simulated field map with the data-driven maps, both need to be compared. Moreover, it needs to be evaluated if the simulation including the charge-up effect describes the data better than the simulation without the charge-up effect (see sec. 3.2). For the comparison, the simulated maps are subdivided into the same bins as the data-driven map and the mean electric field is calculated for each bin. Figures 3.15a and 3.15b show the data-driven map divided by the simulated maps. The data clearly favors the simulation with the charge-up effect over the one without. In the upper part of the TPC, the data-driven field is up to 20% higher than predicted by the simulated map without charge-up effect. On the other hand, the data-driven map and the simulated map including the charge-up effect show less than 10% deviation in most parts. Only at the top of the TPC, the simulation predicts much stronger fields. This finding is further supported by the z-projection of the maps, shown in fig. 3.16. The z-projection of the map is determined by calculating the mean electric field for each row in the r-direction. The reduced dimension of the projected map diminishes the spatial resolution but yields more precision in the direction of the largest non-uniformity of the drift field, thanks to more statistics.
In conclusion, the data-driven map and the simulated map including the charge-up effect are in good agreement, with the exception of the top of the TPC, where the simulation predicts much stronger fields. The good agreement in the control region is to some extent expected due to the scaling of the model with the simulation. Nevertheless, the data-driven map shows the same trend as the simulation also outside the control region and in regions where the drift field is clearly non-uniform, indicating a robust validation of the simulated map.

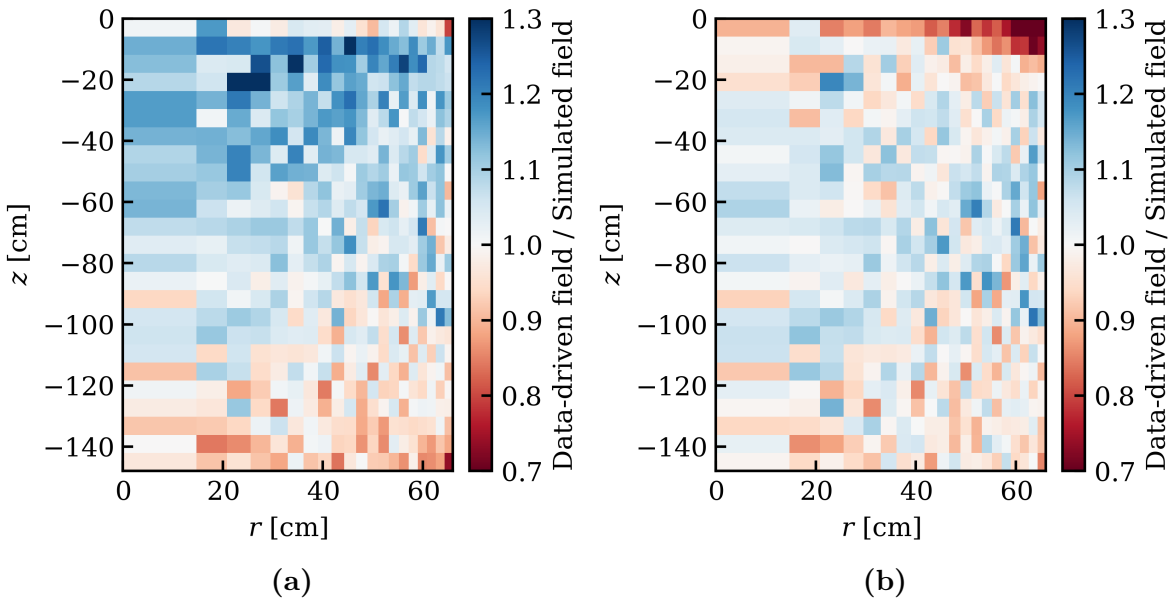

Figure 3.15: Data-driven map divided by the simulated map of the drift field in 2D a) without the charge-up effect and b) including the charge-up effect. The color scales are constrained such that their range is symmetric around one.

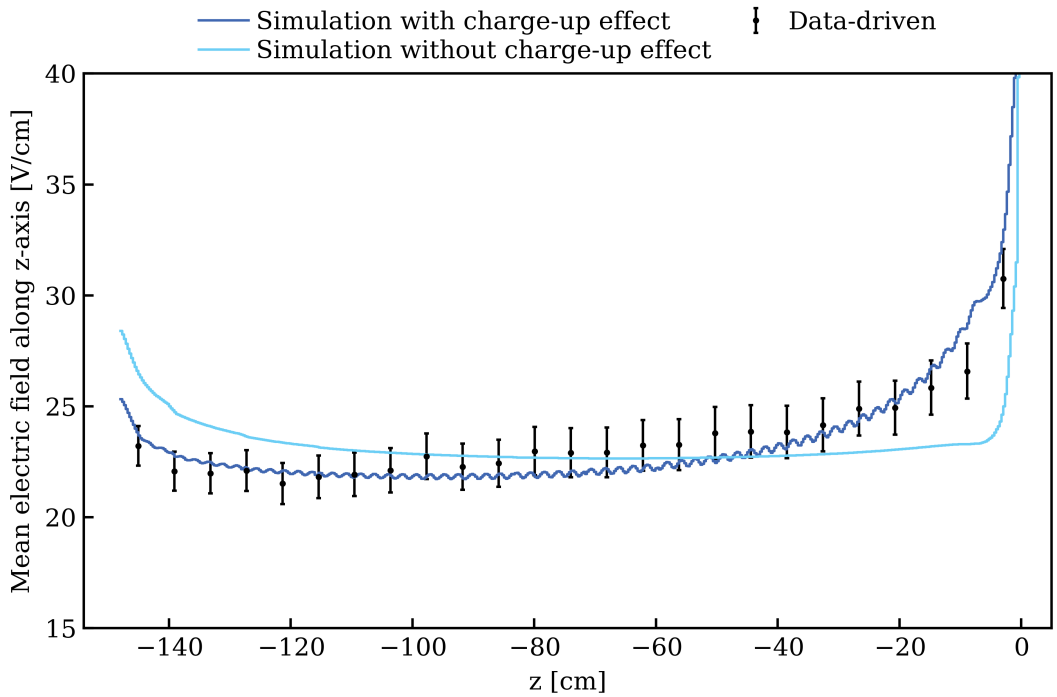

Figure 3.16: Comparison between the simulated field maps with (solid dark blue line) and without charge-up (solid light blue line) and the data-driven map (black markers), shown as a projection of the 2D maps in the vertical z-direction.

3.4 Impact of the non-uniform electric drift field

The results for the reconstructed electric drift field allow to investigate the impact of the non-uniformity of the drift field. As discussed in sec. 2.5, the peak area of the S1 and S2 signals is not corrected for the field dependence. On the one hand, it is not required because the reconstructed energy, the space in which the signal search is performed, is not affected by the non-uniform field. On the other hand, such a correction would be challenging to do, as the field dependence of a signal varies with the interaction type. Electronic recoil and nuclear recoil interactions can be distinguished in the detector, but not β-electrons and γ-rays for example, such that an event-by-event correction would not be possible.
The primary use of the reconstructed field maps is to factor out the field dependence from the applied signal corrections, to avoid that the correction maps are biased by the field dependence of a certain calibration source. Hence, before the correction factors for S1 and S2 are calculated, a field correction map for the calibration source is required. With the reconstructed field map and a model for the field dependence of the calibration source, such as NEST (see sec. 3.3.1), relative correction factors F_c are determined, relating the photon or charge yield for a given field to the yield at the mean field of the detector:

$$F_c = \frac{Y(F(r, \varphi, z))}{Y(F_{mean})}, \tag{3.3}$$

where Y is the charge or photon yield. By dividing $S1$ and $S2$ by F_c, the effect of the non-uniform drift field is removed and the corrections for the electron lifetime, horizontal dependence of S2 and light collection efficiency of S1 can be determined.
Even though the data-driven map and the simulated map show a reasonable agreement, there are some discrepancies, and the required scaling for the reconstruction is subject to uncertainty. The calculation of a potential bias from a wrong field map is beyond the scope of this work, but the impact can be estimated by comparing the field dependence of the signal with the other applied corrections. Therefore, a field correction map for the merged decay of ^{83m}Kr is derived. The events, where the S1 and S2 peaks are merged to yield a combined mono-energetic 41.5 keV signal, are more abundant than the events used for the drift field reconstruction and are the most used for the signal corrections. The HeXe detector does not only provide a model for the field dependence of the peak area ratio, but also for the photon and charge yields of the merged ^{83m}Kr decay with an energy of 41.5 keV [65]. Because of the anti-correlation of charge and photon yield, the corresponding field correction maps are the inverse of each other, and therefore, only the one for the photon yield, and S1 respectively, is derived here.
The resulting correction maps, from both simulation and data are shown in fig. 3.17.

They illustrate that the deviations with respect to the signal at the mean electric field in XENONnT range from -2% to +0.5% in the data-driven map. In the most part of the drift region, the deviations are below ±0.5%. Compared to the non-uniformity of the drift field, ranging from 18 to 40 V/cm in the data-driven map, the deviations of the signal are small. This is even more the case for the comparison with the corrections applied to the S1 and S2 signal. The correction factors for the light collection efficiency of the S1 signal range from around -20% to +50%, as illustrated in fig. 2.7a. The horizontal correction of S2 covers a similar range, though large corrections are only required close to walls and below the perpendicular wires of the gate grid (see fig. 2.7b). Contrary to the other two corrections, in the electron lifetime correction the signal is not normalized to the mean response of the detector but to the initial $S2$ in PE (see sec. 2.5). With an electron lifetime above 10 ms in XENONnT and a maximum drift time of 2.2 ms, the charge loss ranges from 0% to a maximum of 20%. All in all, the variation of the signals due to the non-uniform drift field is small compared to the other position-dependent effects that impact the reconstructed signal.

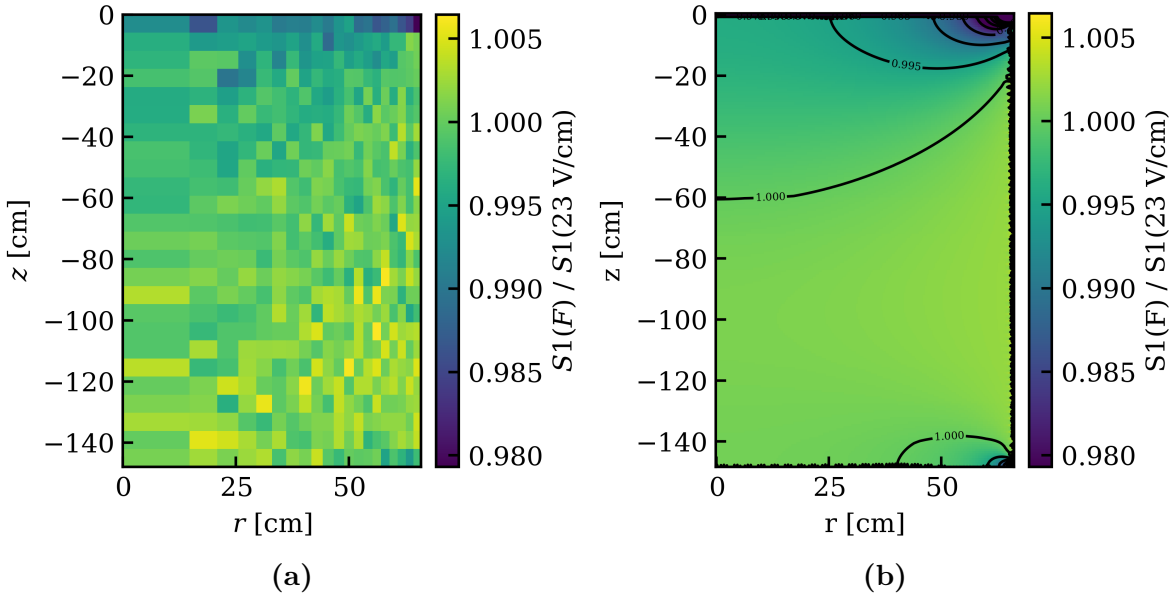

Figure 3.17: Data-driven (a) and simulated (b) field correction map for the merged decay of the calibration source ^{83m}Kr. The yield for the local drift field strength is divided by the yield at the mean field in XENONnT. The color scale covers the whole range of the data-driven map, but is constrained for the simulated map that has very high correction factors close to z = 0 cm.

3.5 Conclusion

In this analysis, the electric drift field in XENONnT was reconstructed with ^{83m}Kr calibration data. The resulting maps of the drift field in 2D and 3D show that the electric field strength can be reconstructed from the peak area ratio $S1_b/S1_a$ of ^{83m}Kr with the empirical HeXe model. However, the model cannot be applied directly to XENONnT but needs to be scaled for the conversion of the ratio to the field strength. The discrepancy between the two detectors arises most likely from differences in the reconstruction process or the delay time distribution of the ^{83m}Kr events, causing a constant global shift. In the future, the delay time dependence of HeXe and XENONnT can eventually be simulated to clarify the origin of the discrepancy. The precision of the data-driven maps is limited by the amount of available ^{83m}Kr data. At the same time, the limited precision is due to the fact that the drift field is highly sensitive to small variations of the peak area ratio. In the middle of the TPC, where the drift field is relatively uniform, the fluctuations as well as the bin size are too large to resolve possible smaller trends. Because of the fluctuations, it is not feasible to use the data-driven map to factor out the field dependence from the signal correction. Until more data is available for the reconstruction, it is better to use the simulated field map for this purpose. Nevertheless, the data-driven map is successfully used to validate the simulated drift field. The data-driven map clearly favors the simulation including the charge-up effect over the one without and shows that this effect needs to be taken into account when simulating the drift field.
With the data-driven map and the validated simulation, the impact of the non-uniformity of the drift field on the signal reconstruction was investigated. The analysis indicates that the drift field is only a minor contributor to the observed inhomogeneity of the signal response in XENONnT before corrections. On the one hand, a field dependence of the reconstructed energy can be avoided by removing the dependence from the applied signal corrections with help of the drift field map. On the other hand, the non-uniformity has only a small impact on the amount of measured light and charge. A field correction map for the merged decay of ^{83m}Kr was obtained to serve as an estimate of the impact. It shows that the non-uniform drift field has small influence on the reconstructed signal, compared to other inhomogeneities of detector, like the light collection efficiency or the signal attenuation by electronegative impurities in liquid xenon. This is especially true inside the fiducial volume, where the drift field is relatively uniform.

Chapter 4

Search for radiation from wave function collapse

The low background, low energy threshold and large target mass of XENONnT offer the opportunity to search for the x-ray emission from wave function collapse and test the CSL model and the gravity-related DP model presented in chapter 1. Thereby, the xenon of the detector serves as emitter and as target for the detection of the x-rays at the same time. The predicted radiation would produce electronic recoils in the dual-phase TPC. To search for this signal, this work makes use of the analysis framework that XENONnT developed for the search of physics beyond the Standard Model in electronic recoil interactions. In July 2022, XENONnT presented results of the analysis of electronic recoil data from the first science run, setting stringent exclusion limits on solar axions, an enhanced neutrino magnetic moment and bosonic dark matter [4]. The search for x-ray emission from wave function collapse is performed with the same dataset.

The chapter is organized as follows: In sec. 4.1 the theoretical emission rate for the CSL and the DP model, and the energy region of interest is introduced. The data selection and the calculation of the efficiency is described in sec. 4.2. Section 4.3 presents the background model and sec. 4.4 the statistical inference of the signal search. The results for the test of the CSL and the DP model are reported in 4.5 and discussed in 4.6.

4.1 Emission rate and signal model

The collapse dynamics of the CSL and DP model imply that charged particles would constantly emit radiation, predominately in the x-ray regime. Due to the similar

structure of the modified Schrödinger equations of the two models shown in sec. 1.2, the predicted emission rates of both models have a $1/E$ energy dependence.
For the CSL model, earlier studies derived the emission rate for a free electron and applied it to the outer electrons of an atom, considered as quasi-free [70]. More recently, an equation for a generic system of non-relativistic charged particles was derived that can be used to describe the radiation emission of all charged constituents of an atom. The differential rate for a system of N particles with charge q_i is given by [33]

$$\frac{d\Gamma(E)}{dE} = A \cdot \frac{\hbar\lambda}{4\pi^2\epsilon_0 m_0^2 c^3 r_c^2} \cdot \frac{1}{E}, \tag{4.1}$$

where $\hbar$ is the reduced Planck constant, ϵ_0 is the vacuum permittivity, c is the speed of light and m_0 is the nucleon mass. The collapse rate λ and the correlation length r_c are the phenomenological parameters of the CSL model. The charge amplification factor A differs depending on whether the N particles emit coherently or incoherently. If each particle radiates independently, then the emission is incoherent and $A = \sum_{i=1}^{N} q_i^2$. This is given when the typical distance between each particle is larger than the wavelength λ_k of the emitted radiation. If the particles are separated less than λ_k, then the emission is coherent, such that the N particles radiate like a single particle and $A = (\sum_{i=1}^{N} q_i)^2$. From these two types of emission it follows that the emission rate of an atomic system is maximized for a certain range of wavelengths. First, the electrons and protons of an atom should emit incoherently, otherwise, their respective radiations would cancel due to their opposite charge. Hence, only λ_k smaller than the atomic radius $\sim 10^{-1}$ nm are considered. Second, the protons inside a nucleus should emit coherently, such that their contribution scales quadratically with the number of protons. Hence, only λ_k larger than the nuclear radius $\sim 10^{-5}$ nm are considered. This range of wavelengths $\lambda_k \sim 10^{-5} - 10^{-1}$ nm corresponds to the energy range $E \sim 10 - 10^5$ keV. However, the subdominant linear contribution from the electrons, proportional to Z, can only be considered for non-relativistic energies due to the non-relativistic derivation of eq. 4.1. The total emission rate for a detector with a target mass M, the number of atoms per unit mass n, and the atomic number of the target material Z is then given by

$$\frac{d\Gamma_{\mathrm{CSL}}(E)}{dE} = n \cdot M \cdot (Z + Z^2) \cdot e^2 \cdot \frac{\hbar\lambda}{4\pi^2\epsilon_0 m_0^2 c^3 r_c^2} \cdot \frac{1}{E}. \tag{4.2}$$

For the DP model, the considerations about the energy range for the emission rate of an atomic system are also valid, yielding a similar emission rate with different charac-

teristic constants [38]:

$$\frac{d\Gamma_{\mathrm{DP}}(E)}{dE} = n \cdot M \cdot (Z + Z^2) \cdot e^2 \cdot \frac{2G}{3\pi^{3/2}\epsilon_0 c^3 R_0^3} \cdot \frac{1}{E}, \tag{4.3}$$

where G is the gravitational constant and R_0 the regularization scale of the DP model, that needs to be determined experimentally.
The emission rates of the two models define the energy spectra that are used as signal models for the analysis. Considering the energy range, XENONnT has an energy threshold as low 1 keV. This would allow performing the search for energies above 10 keV, where the protons and electrons start to emit radiation independently. However, discussions with the authors of [33] revealed that the rate in eq. 4.2 and 4.3 is overestimated close to the lower bound of 10 keV because the transition from coherent to incoherent emission is continuous and not discrete. Currently, no theoretical model is available that describes the expected rate at these low energies. Therefore, this analysis uses the same lower energy bound as the MAJORANA experiment, corresponding to 19 keV [34]. This allows for a comparison of XENONnT with MAJORANA that has set the most stringent exclusion limits on the CSL and the DP model so far, as shown in sec. 1.3. The upper bound for this analysis is 140 keV, defined by the provided background model for electronic recoils in XENONnT. Due to the $1/E$ energy dependence of both models, the high-energy cutoff is not expected to significantly reduce the sensitivity of this analysis. In conclusion, the energy region of interest for this analysis is between 19 and 140 keV.
This analysis constitutes the first search for radiation from wave function collapse with a xenon-based detector. Compared to germanium, that was employed in the previous experiments, xenon has a higher expected x-ray emission rate: Although xenon has a smaller number of atoms per unit mass n than germanium [71], the larger atomic number of Z=54 compared to Z=32 results in a 1.6 times higher emission rate, following eq. 4.2. However, the main advantage of XENONnT in terms of the expected rate is its large target mass $M = 4.37$ t inside the fiducial volume, that is around 100 times the target mass employed in MAJORANA.

4.2 Data selection and efficiency

The dataset used for the search was collected during the first science run of XENONnT between July and November 2021 [4]. After removing the data taken during calibrations and unstable detector conditions, the total livetime of data collection amounts to 97.1 days. A variety of selection criteria are applied to ensure data quality and to

improve the signal to background ratio in the data. Data quality cuts aim to ensure a selection of valid pairs of S1 and S2 signals. The cuts target mis-classified and falsely paired signals, based on event parameters, such as the S1 and S2 widths, PMT hit patterns and reconstructed position [49]. The background is reduced by selecting only electronic recoil events in the $cS1$-$cS2$ parameter space. Thereby, nuclear recoil events are removed as well as background events from the PTFE walls of the TPC that is contaminated by ^{222}Rn progeny [59]. When these decay on a PTFE wall charge losses occur and move events outside of the ER band. Multiple scatter events are removed because the radiation from wave function collapse in the x-ray regime is expected to deposit the whole energy in one interaction. The total efficiency for the detection of signal-like events is the combination of the detection efficiency, driven by the smallest size of S1 and S2 peaks that XENONnT can measure, and the efficiencies of the event

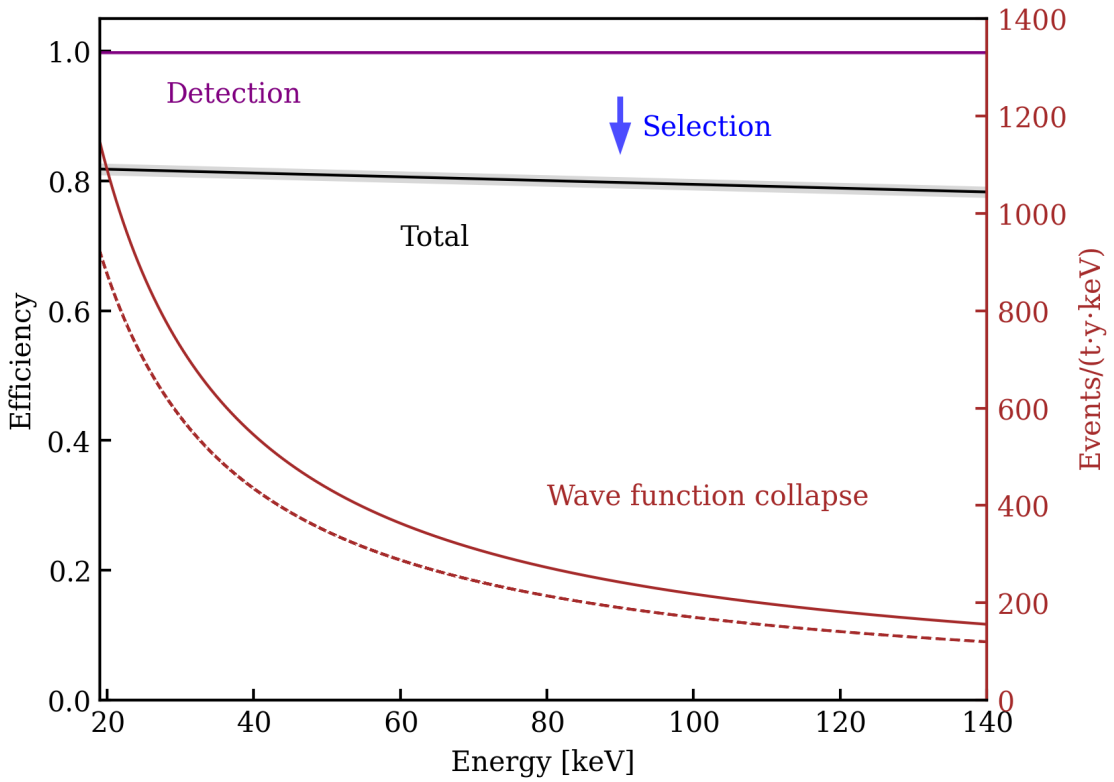

Figure 4.1: Efficiency in the region of interest between 19 and 140 keV. The detection efficiency (black line) in combination with the event-selection efficiencies yields the total efficiency (black line). The uncertainty for the total efficiency is shown as a shaded band. The solid and dashed red line indicate the x-ray signal spectrum from wave function collapse before and after applying the efficiency and energy resolution, respectively. The signal rate is given by the currently most stringent limit for the parameters λ and r_c of the CSL model [34]. Figure adapted from [4].

selection cuts. Figure 4.1 shows the detection efficiency as well as the combined total efficiency. Whereas the total efficiency approaches zero close to the detector's energy threshold of 1 keV, it is around 80% and almost flat in the region of interest of this analysis. The detection efficiency is close to 100% in the energy region of interest and was determined by simulations and validated with ^{37}Ar and ^{220}Rn calibration data [4]. To determine the selection efficiency, the acceptance of all selection cuts was evaluated with calibration and background data, as described in [49].
Finally, the dataset is restricted to events inside the fiducial volume. The shape of the volume was optimized to achieve a low background, by removing the events close to the TPC walls and the liquid-gas interface, and at the same time a large target mass. The selected fiducial volume of 4.37 t combined with the livetime of 97.1 days, yield a total exposure of 1.16 tonne-years. After applying all selection cuts, 3335 observed events remain in the dataset with energies between 19 and 140 keV.

4.3 Background model

To test the signal hypothesis of x-ray emission from wave function collapse, a precise background model B_0 is required that serves as the null-hypothesis in the statistical inference. In the energy region of interest, the background model of XENONnT consists of eight components, listed in tab. 4.1 [4]. For five of them, there are constraints on the expected number of events from independent measurements. The constraints are taken into account for the fit of the data. While the background model B_0 was developed, the data in the electronic recoil signal region was blinded below 20 keV.
At low energies, the flat spectrum from the β decay of ^{214}Pb is expected to dominate the background. As mentioned in sec. 2.1, ^{214}Pb is in the decay chain of ^{222}Rn, which is continuously emanated from detector materials. By measuring the activity of the parent and daughter isotope ^{218}Po and ^{214}Po, a lower and upper bound is obtained for the number of expected events of ^{214}Pb in XENONnT. The second β-emitter ^{85}Kr is an intrinsic contaminant of xenon. The measured concentration of (56 $\pm$ 36) ppq $^{\text{nat}}$Kr in xenon together with the abundance of ^{85}Kr in $^{\text{nat}}$Kr as well as the half-life allow to predict the expected background rate [4]. The background contribution from the detector materials is induced by γ-rays reaching the fiducial volume. The γ decays are simulated with the software Geant4 [72], using the results from the radioassay measurements of the detector components [42]. The simulation shows that the material background can be modeled with a flat energy spectrum in the region of interest and yields an estimation for the rate. The two-neutrino double-beta ($2\nu\beta\beta$) decay of ^{136}Xe is expected to dominate the background spectrum at higher energies. The abundance

Table 4.1: Electric recoil background components in the energy the region of interest (19, 140 keV). The constraints and the best-fit values of B_0 are given in terms of the total number of observed events after the efficiency loss.

Component	Constraint	Fit for B_0
^{214}Pb	$(513, 1118)$	818.2 ± 120.6
^{85}Kr	78.2 ± 50.8	79.4 ± 50.5
Materials	232.1 ± 44.2	233.0 ± 43.9
^{136}Xe	1507.0 ± 55.2	1491.8 ± 53.6
Solar neutrino	245.9 ± 24.6	247.7 ± 23.9
^{124}Xe	-	248.1 ± 28.1
^{133}Xe	-	146.4 ± 66.9
^{83m}Kr	-	74.6 ± 16.1

of the isotope in xenon was measured to be 9%, allowing to determine a constraint with the half-life of ^{136}Xe. The theoretical spectrum of the decay is subject to uncertainty due to the intermediate nuclear states. The mean of the higher state dominance and the single state dominance spectrum is implemented and the uncertainty is taken into account with a shape parameter (see sec. 4.4). The background originating from the elastic scattering of solar neutrinos on electrons is the last component with a fit constraint. The spectrum is modeled from the solar pp-neutrino flux and the interaction cross section [73]. The rate uncertainty is set to 10%, informed by the currently most precise pp-flux measurement from Borexino [74]. The intrinsic isotope ^{124}Xe decays via a double-electron capture process. The spectrum consists of several peaks originating from captures from different atomic shells of ^{124}Xe. The last two components ^{133}Xe and ^{83m}Kr are residuals from calibrations. Although datasets within 24 h of a ^{83m}Kr calibration are not used for analysis, with its 1.83 h half-life, ^{83m}Kr is present in small amounts in subsequent data. The spectrum of ^{83m}Kr is defined by a peak at 41.5 keV, as shown in sec. 2.4. ^{133}Xe decays via β decay with a coincident γ and was produced by neutron capture in the ^{241}AmBe calibration that was conducted before the first science run.

The background model B_0 is used to fit the selected electronic recoil data in the space of reconstructed energy with an unbinned profile likelihood fit that is described in detail in the next sec. 4.4. The best fit shows a good agreement with the data in fig. 4.2. The extracted number of events for each component are indicated in tab. 4.1. The

largest contribution over the whole energy range originates from ^{136}Xe. However, at low energies, where the x-ray signal rate is predicted to be the largest, ^{214}Pb dominates. The ^{83m}Kr contamination yields a non-negligible contribution. In the future, this could be omitted by extending the exclusion period of post-calibration data, at the cost of a loss of exposure.

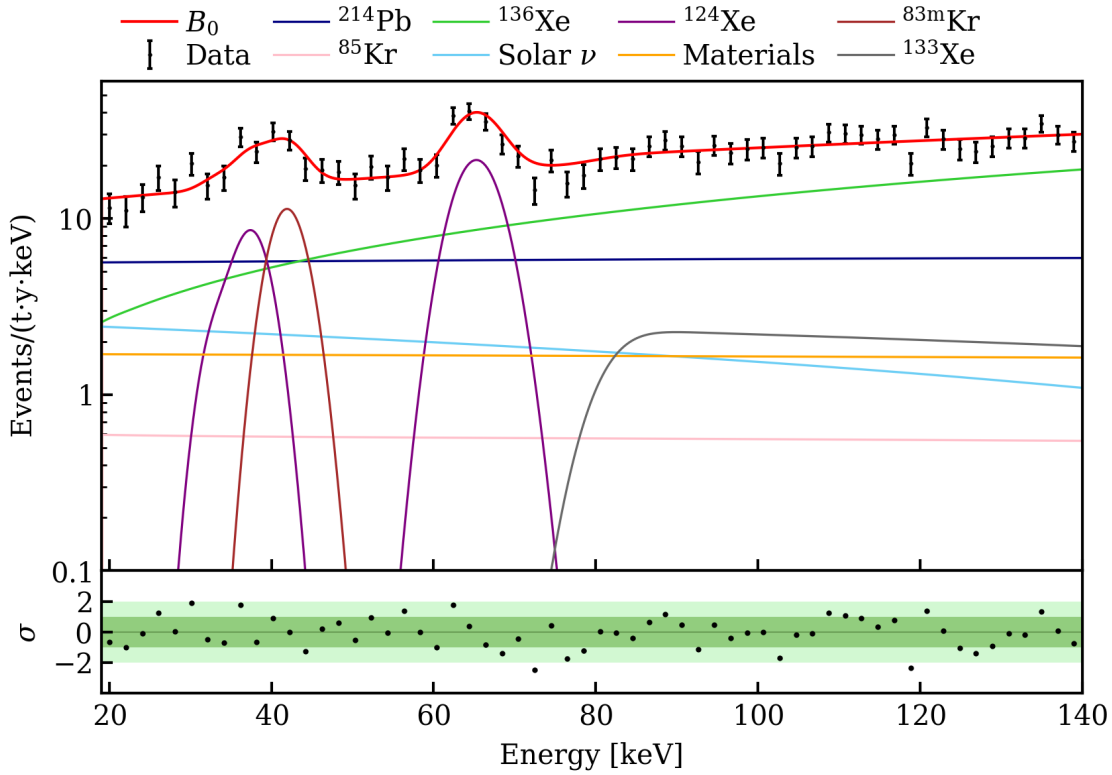

Figure 4.2: Top panel: best fit of the electronic recoil data for the background model B_0. The colored lines represent the results from the unbinned fit, whereas the data is shown as a histogram with a binning of 2 keV. Bottom panel: residuals of the fit normalized by the uncertainty on the number of events N_i in each bin, given by $\sqrt{N_i}$.

4.4 Statistical inference

The inference for the search of radiation from wave function collapse is based on an unbinned profile likelihood method implemented in the low-energy electronic recoil analysis software package that is used for this analysis [73, 75]. It allows to fit the signal and background model, test the signal hypothesis and set limits on signal rates.

The unbinned likelihood is defined as follows:

$$\begin{aligned}\mathcal{L}\left(\mu_s, \boldsymbol{\mu_b}, \boldsymbol{\theta}\right) = &\,\text{Poiss}\left(N \mid \mu_{tot}\right) \\ &\times \prod_i^N \left(\sum_j \frac{\mu_{b_j}}{\mu_{\text{tot}}} P_{b_j}\left(E_i, \boldsymbol{\theta}\right) + \frac{\mu_s}{\mu_{\text{tot}}} P_s\left(E_i, \boldsymbol{\theta}\right) \right) \\ &\times \prod_m \left(C_{\mu_m}\left(\mu_{b_m}\right)\right) \times C_\theta, \\ \mu_{\text{tot}} \equiv &\sum_j \mu_{b_j} + \mu_s.\end{aligned} \tag{4.4}$$

The likelihood is a function of the total number of expected signal events μ_s and the nuisance parameters $\boldsymbol{\mu_b}$ and $\boldsymbol{\theta}$, whereby $\boldsymbol{\mu_b}$ is a vector of the expected events for all background components and $\boldsymbol{\theta}$ is the vector of the shape parameters for the uncertainty on the efficiency. The probability distribution functions (PDFs) of the backgrounds and the signal are denoted as P_{b_j} and P_s, respectively. The background PDFs are defined by the shape of the energy spectra discussed in sec. 4.3. The CSL and DP signal models share the the same PDF, as their spectra display the same energy dependence of $1/E$ (see fig. 4.1). For each of the N observed events, the sum of all PDFs is calculated with the corresponding energy of the event E_i. Index j runs over all background components. The constraints on the expected number of background events, listed in tab. 4.1, are denoted as C_{μ_m} and are multiplied with the summed PDFs. Except for the background ^{214}Pb, all constraints are represented by a Gaussian whose mean and standard deviation are given by the expected number of events and the uncertainty. The constraint for ^{214}Pb is represented by a uniform distribution with a lower and upper bound. C_θ is a shape parameter for ^{136}Xe, allowing the fit to vary between the two theoretical spectra.
By maximizing the likelihood, the best-fit number of signal and background events is obtained. For the fit of B_0 shown in fig. 4.2, the signal parameter μ_s is set to zero. To evaluate the significance of the signal hypothesis H_1 compared to the background-only hypothesis $H_0 = B_0$, the following test statistic [76]

$$q\left(\mu_s\right) = -2 \ln \frac{\mathcal{L}\left(\mu_s, \hat{\hat{\boldsymbol{\mu}}}_b, \hat{\hat{\boldsymbol{\theta}}}\right)}{\mathcal{L}\left(\hat{\mu}_s, \hat{\boldsymbol{\mu}}_b, \hat{\boldsymbol{\theta}}\right)} \tag{4.5}$$

is used, where $\left(\hat{\mu}_s, \hat{\boldsymbol{\mu}}_b, \hat{\boldsymbol{\theta}}\right)$ is the set of parameters corresponding to the best fit, yielding the unconditional maximum likelihood. The parameter set $\left(\mu_s, \hat{\hat{\boldsymbol{\mu}}}_b, \hat{\hat{\boldsymbol{\theta}}}\right)$ maximizes the likelihood for a fixed number of signal events μ_s. The statistical discovery significance is then given by $q(0)$. The distribution of the test statistic $q(\mu_s)$ can be approximated,

under a set of conditions, with a χ^2 distribution with one degree of freedom [77]. This allows to compute an upper limit on μ_s with a critical value for $q(\mu_s)$ that corresponds to a certain confidence level (C.L.). In this analysis, the 95% C.L. upper limit is derived to compare the results of this analysis to previous tests of the CSL and the DP model. Thereby, the upper limit on the number of signal events can be converted into limits on the phenomenological parameters of the two signal models, using eq. (4.2) and eq. (4.3). The upper limit requires a one-sided test statistic that is given by

$$\tilde{q}(\mu_s) = \begin{cases} q(\mu_s) & \text{if } \mu_s > \hat{\mu_s}, \\ 0 & \text{else.} \end{cases} \tag{4.6}$$

In the asymptotic case, the upper limit $\mu_{s(95\%)}$ is obtained by scanning $\tilde{q}(\mu_s)$ for the critical value $\tilde{q}(\mu_{s(95\%)}) = 2.71$ [75]. However, to ensure that the upper limit has the correct coverage, the asymptotic approximation needs to be validated with toy Monte Carlo (toy MC) simulations. The coverage is defined as the fraction of repeated experiments where the true number of signal events is smaller than the obtained upper limit [59]. If the coverage is larger than the targeted 95%, it is referred to as over-coverage, in the opposite case as under-coverage.

Check of coverage and critical value

To estimate the coverage for a certain true number of signal events, repeated experiments are simulated with toy MC datasets. The datasets consist of simulated background and signal events. For each dataset, the upper limit $\mu_{s(95\%)}$ is determined using the asymptotic critical value and compared to the true injected signal rate. The datasets are simulated by drawing for the signal and each background component a Poisson sample of the expected number of events. The energies of the signal and background events are distributed according to the respective PDFs. The number of expected events for each background component is based on the best fit of B_0 that was evaluated in the energy region between 30 and 140 keV before the collected data was unblinded. The coverage is determined for several true signal rates with 300 toy MC datasets per data point for the injected rate. The results in fig. 4.3a show a slight over-coverage for the best-fit number of signal events of H_1, discussed in the next sec. 4.5. However, the results are limited at this point by the fact that the uncertainties are unknown. The calculation of the uncertainties was beyond the scope of this work but should be done in a future study.
A second check is performed, estimating the true critical value for the 95% C.L. from the distribution of $\tilde{q}(\mu_{s(true)})$. In the same way as for the coverage check, toy MC

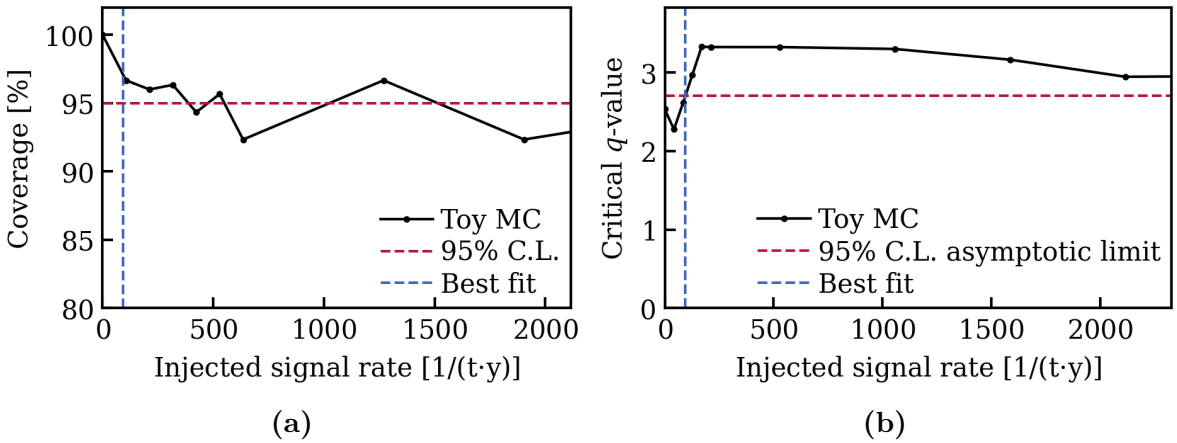

Figure 4.3: a) Coverage for the 95% C.L. upper limits on the x-ray signal rate from wave function collapse. The true injected signal rate is indicated per exposure. Each point is based on 300 simulated toy MC datasets. (b) Simulation of the true critical value at 95% C.L. for the same signal with 2000 toy MC datasets per true signal rate. The blue dashed line in both figures represents the best fit for the signal in the measured data.

datasets are sampled that contain a number of signal events. For each dataset the test statistic $\tilde{q}(\mu_{s(true)})$ is determined, whereby $\mu_{s(true)}$ is the true injected number of signal events. The 95% percentile of the distribution $\tilde{q}(\mu_{s(true)})$ then yields an estimate of the true critical value, shown in fig. 4.3b. As this simulation requires around six times less computation time than the simulation of the coverage, 2000 toy MC datasets are sampled per signal rate. The critical values increase from below the asymptotic limit, cross it close to the best-fit, and approach it for a large number of signal events. The critical values should display the opposite trend than the obtained values for the coverage. Figures 4.3a and 4.3b indicate that this is not always the case. However, the deviation can probably be explained by the different amount of statistics for the two checks and the unknown uncertainties. Based on the estimation for the true critical value, which relies on more statistics, the asymptotic limit is used for this analysis.

4.5 Results

The result of the search for x-ray emission with electronic recoil data of XENONnT is presented in fig. 4.4. The best fit is shown for the combined signal and background model H_1 as well as for the signal and each background component.

The best-fit value for the total number of signal events per exposure between 19 and 140 keV is 93^{+108}_{-93} events/(t·y) before the efficiency loss. However, no significant signal

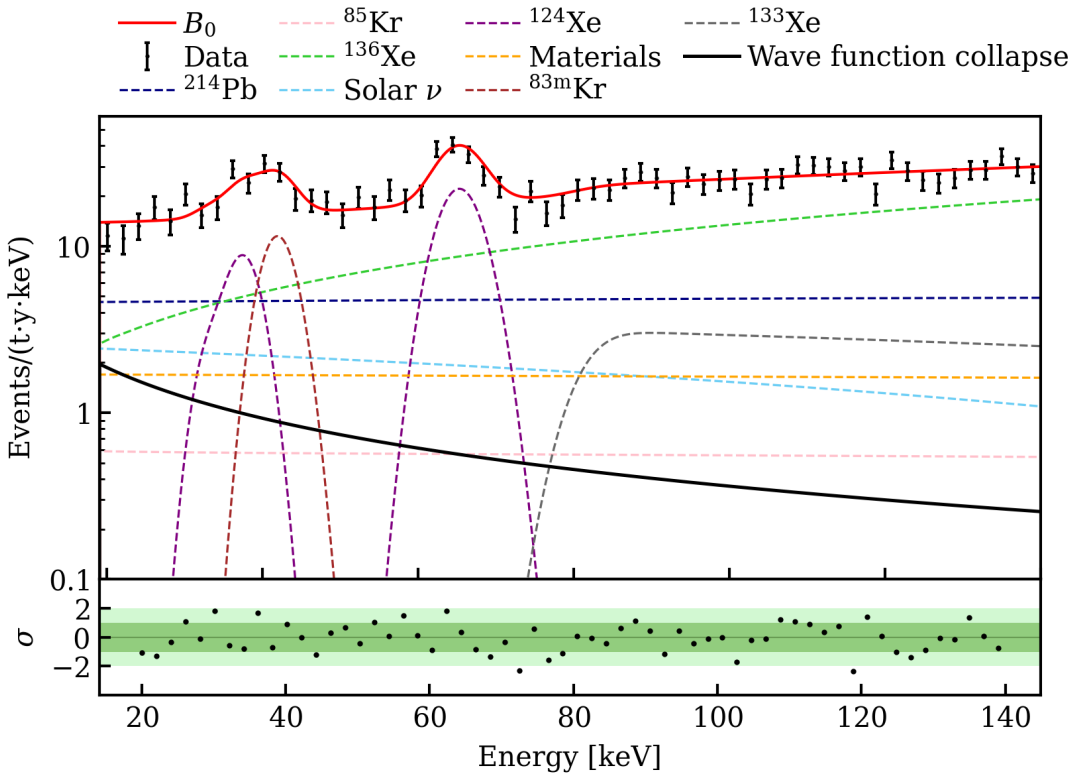

Figure 4.4: Top panel: best fit of the electronic recoil data for the combined background and signal model H_1 (red solid line). The colored dashed lines represent the backgrounds, the solid black line the radiation from wave function collapse, and the data is shown in the form of a histogram with a binning of 2 keV. Bottom panel: residuals of the fit normalized by the uncertainty on the number of events N_i in each bin, given by $\sqrt{N_i}$.

was observed with a significance of 0.73σ for H_1 compared to B_0. The comparison with the best fit of B_0 in fig. 4.2 shows that primarily the background rate from ^{214}Pb is reduced at low energies for H_1, allowing for a small signal with a maximum of 2 events/(t · y · keV). At high energies, the rate of ^{133}Xe is slightly increased. The large uncertainty on the signal rate can be explained by the relatively unspecific signature of the wave function collapse signal, allowing for larger variations of the fit within the uncertainty bounds. Figure 4.5 shows the test statistic $q(\mu_s)$ with the best fit and the corresponding 1σ uncertainty band[1].

As explained in sec. 4.4, the 95% C.L. upper limit is determined by scanning the one-sided test statistic $\tilde{q}(\mu_s)$ for the asymptotic critical value $\tilde{q}(\mu_{s(95\%)}) = 2.71$. The critical value corresponds to the upper limit of $\mu_{s(95\%)} = 268$ events/(t·y). This result can be converted into limits on the phenomenological parameters of the CSL and the DP model. For the the collapse rate λ and the correlation length r_c of the CSL model,

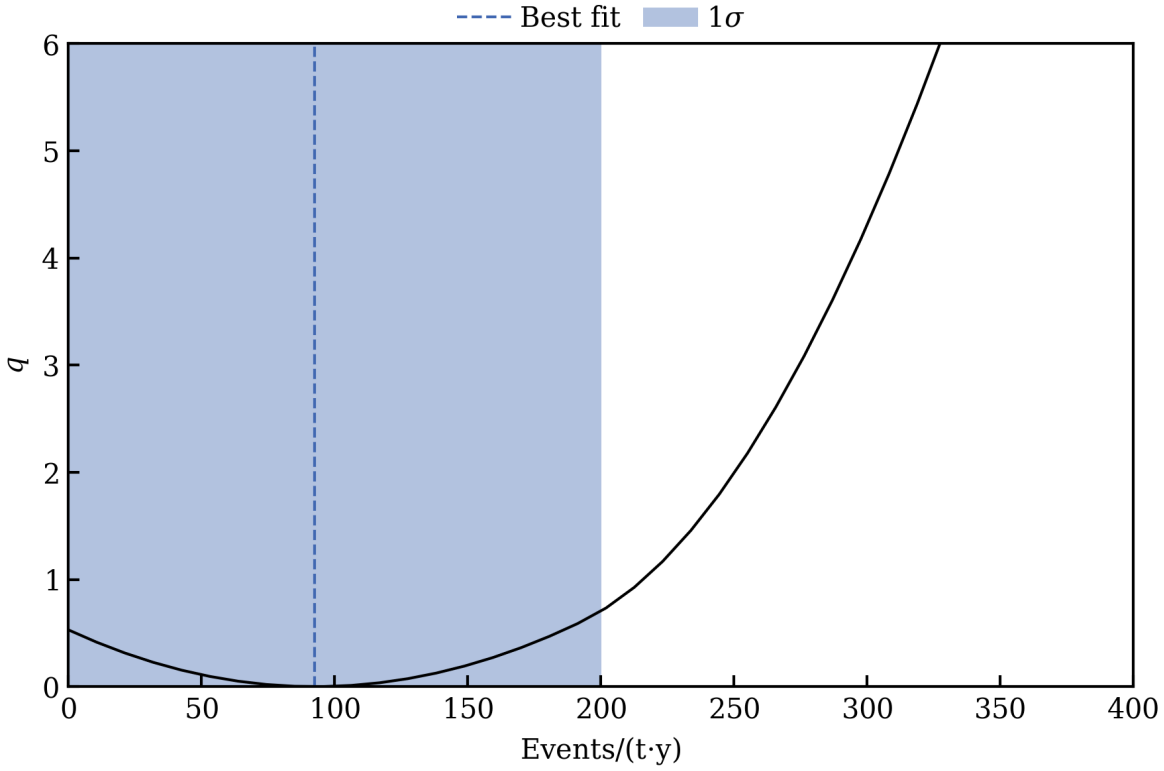

Figure 4.5: Log likelihood ratio curve as a function of the signal rate.

eq. (4.2) yields the limit

$$\lambda/r_c^2 < 3.04 \times 10^{-3}\ \mathrm{s}^{-1}\mathrm{m}^{-2}.$$

For the DP model, the upper limit on the signal rate converts into a lower limit for the regularization parameter R_0. Following eq. (4.3) yields the limit

$$R_0 > 1.4 \times 10^{-9}\ \mathrm{m}.$$

4.6 Discussion

The reported results for the search of radiation from wave function collapse represent stringent tests of the CSL and the DP model. For the CSL model, this work sets the most stringent upper limit for correlation lengths of $r_c < 10^{-5}$ m by excluding the parameter space $\lambda/r_c^2 > 3.04 \times 10^{-3}\ \mathrm{s}^{-1}\mathrm{m}^{-2}$ at 95% C.L. Figure 4.6 shows the new constraint in comparison with other theoretical and experimental exclusion limits. Compared to the MAJORANA [34], that set the previous best limit for the x-ray emission, the upper limit obtained is an improvement by a factor of 162. For the DP model, this work sets the most stringent lower limit on the regularization scale R_0 by

[1]The uncertainty on the best-fit signal is derived by scanning the test statistic above the best-fit for the rate where $q(\mu_s) = 1$ and dividing it by 2. This is owed to the fact the the likelihood is undefined for negative signals such that a symmetric interval where $q(\mu_s) = 1$ cannot be constructed. This does not affect the upper limit.

excluding values below 1.4×10^{-9} m at 95% C.L. This is an improvement by a factor 2.8 compared to the previous best limit by MAJORANA. In contrast to the CSL model, the improvement is more modest for the DP model due to the weaker dependence of R_0 on the radiation emission rate.
In general, the improvement of XENONnT compared to MAJORANA does not only rely on the 1.6 times higher emission rate of xenon compared to germanium and the

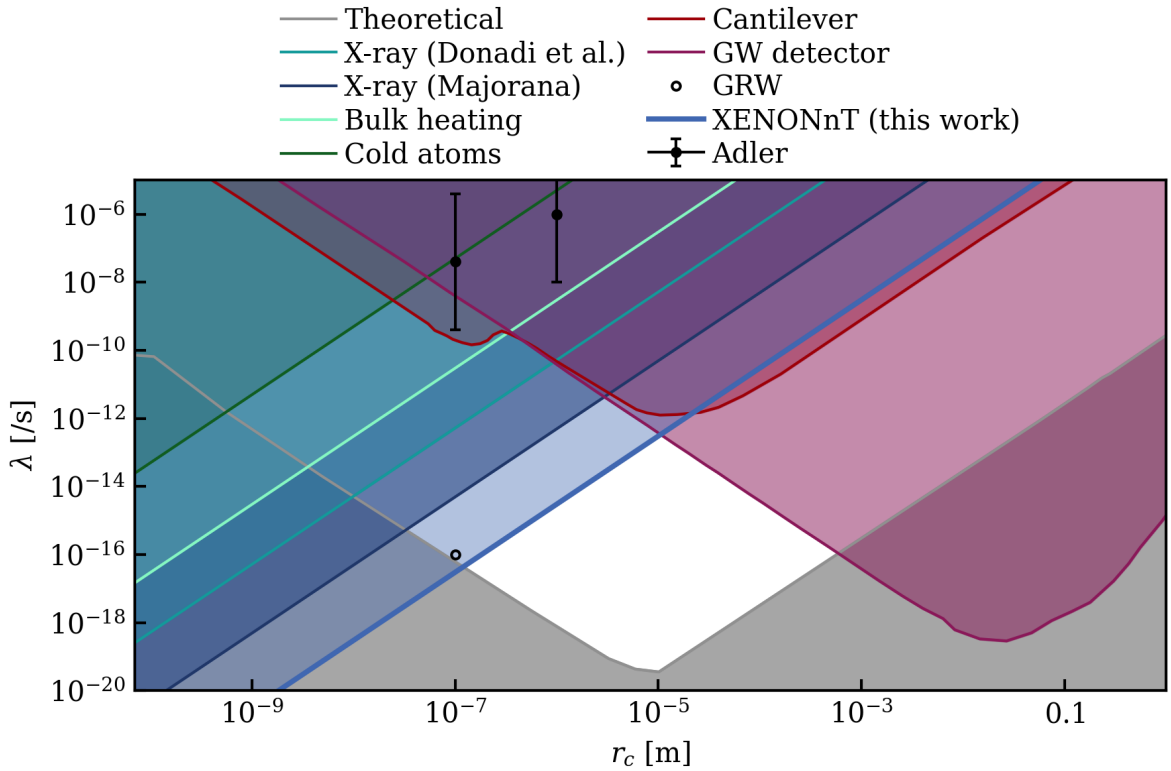

Figure 4.6: Exclusion limits for the CSL collapse parameters λ and r_c from non-interferometric experiments and theoretical propositions. The upper bound obtained by this work is shown as a solid blue line. The upper bound from the gravitational wave (GW) detector LISA Pathfinder [29, 30] excludes the purple shaded parameter space. The red exclusion area is obtained from a cantilever experiment [31], the green area is from a cold atoms experiment [28], and the blue-green area is derived from the measured heating rate in the CUORE experiment [32]. The two previous limits from searches for x-ray emission are set by Donadi et al. (light blue) [33] and MAJORANA (dark blue) [34]. The black dots and the circle represent the theoretical values suggested by Adler [18] and GRW [15], respectively. The theoretical lower bound excluding the gray area is based on the following requirement: a graphene disk of the minimum size a human eye can resolve ($\simeq$ 0.01 mm) should be localized faster than the human eye's perception time ($\simeq$ 10 ms) [26]. The white area is the parameter space not yet excluded.

31 times higher exposure, but also on a lower background rate that was achieved by several reduction measures. At low energies, where the x-ray signal rate is predicted to be the largest, the dominating electronic recoil background originates from ^{214}Pb in XENONnT. In the future, this contribution will be further reduced due to an upgrade of the XENONnT radon removal system discussed in sec. 2.1 [4, 43].
The exclusion limits from both this work and from MAJORANA are subject to the theoretical uncertainty on the emission rate at low energies, as discussed in sec. 4.1. Due to the transition from incoherent to coherent radiation emission at around 10 keV, the CSL and DP emission rate for atomic systems and consequently the calculated upper limits are likely overestimated in this energy region. This might also hold around the lower bound of the region of interest, but cannot be precisely quantified at this time. According to the authors of [33], a new theoretical model that describes the expected rate at low energies is expected to deliver a more specific spectral shape than the 1/E spectrum. This would allow better discrimination between backgrounds and the potential signal. Furthermore, it could allow to probe the signal below the applied lower bound of 19 keV and make use of the low energy threshold of XENONnT. Hence, an adapted model for the x-ray emission in the few keV region could weaken the set exclusion limits if it predicted a lower emission rate around the lower bound of the chosen energy region of interest in this work. This could, however, be compensated by extending the region of interest to the low-energy threshold of XENONnT. Therefore, a reanalysis of the XENONnT data presented in this work makes sense once an extended model is available.
With the $1/E$ model, the upper limit on λ/r_c obtained in this work rejects not only the parameters suggested by Adler [18], but is the first to reject the parameters suggested by Ghirardi, Rimini and Weber [15]. The two phenomenological parameters define at which scale the collapse terms become dominant and suppress macroscopic superposition. Combined with the constraints from gravitational wave detectors, the obtained limit also rules out the largest part of the parameter space defined by the theoretical (gray) bound that is based on the collapse time for a small graphene disk. This makes the CSL model in its standard formulation increasingly unlikely and motivates the experimental test of theoretical extensions of the model, described in sec. 1.2.1. The colored CSL model as well as the dissipative CSL model introduce new parameters and thus widen the parameter space. With the demonstrated sensitivity, XENONnT will be able to contribute to the test of these models. The interpretation of results for the DP model is open at this point. Like previously established limits, the obtained limit rejects the hypothesis that R_0 can be identified with the size of a particle's mass density and thus the parameter-free version of the DP model [38].

Conclusion and outlook

Wave function collapse models address the long-standing measurement problem of quantum mechanics. They introduce a collapse mechanism that causes a breakdown of quantum superposition at the transition from the microscopic to the macroscopic realm. This work reports on a search for the radiation from wave function collapse with the XENONnT dark matter experiment focusing on the continuous spontaneous localisation (CSL) model and the gravity-related Diósi-Penrose (DP) model. Both models predict the emission of x-rays by matter as a consequence of the proposed collapse mechanisms. The emission rate is proportional to the number of emitting atoms and is the largest in the low keV energy region, requiring a detector with a large target mass and a low energy threshold.

XENONnT accomplishes these requirements with a design optimized for the direct detection of dark matter, providing a xenon target of 5.9 t and a 1 keV energy threshold. The experiment employs a dual-phase time projection chamber (TPC) to measure the light and charge signal generated by energy depositions in the detector. Due to different position-dependent effects, the detector's response to an energy deposition is not uniform. This is addressed by different corrections to the reconstructed signals. One contributor to the observed non-uniformity of the detector's signal response is the electric drift field that is applied to measure the charge signal.

This work reconstructed the electric drift field across the entire TPC with ^{83m}Kr calibration data to quantify the variation of the drift field and investigate how it affects the reconstructed signal. Two and three dimensional maps of the drift field were produced by using the two light signals from the two-staged decay of ^{83m}Kr. The maps show that the drift field is relatively uniform in the middle of the TPC but increases towards the bottom and top. The maximum variation compared to the mean drift field ranges form -20% to +70%. However, it was found that the observed non-uniformity has only a small impact on the amount of measured light and charge and that the corresponding

field corrections are of the order of 0 to 2% and subdominant compared to other signal corrections. For the reconstructed energy of an interaction, the impact can be avoided entirely by removing the field dependence from the signal corrections. The employed data-driven method is limited in precision by the amount of calibration data available, but proved useful to validate simulated maps of the drift field.

To search for radiation from wave function collapse, this work implemented the signal model of the CSL and the gravity-related DP model into the analysis framework from XENONnT for low-energy electronic recoil searches. The signal hypothesis was tested against the background-only hypothesis with an unbinned profile likelihood method. In the energy region of interest (19, 140) keV, the background model is defined by the energy spectra of eight background components, of which five are constrained by independent measurements. The signal spectrum is defined by the $1/E$ energy dependence of the radiation emission rate that is shared by the CSL and the DP model. The electronic recoil dataset used for the search was recorded during the first science run of XENONnT and yields 1.16 tonne-years of exposure.

The search in the electronic recoil data showed no significant signal consistent with radiation from wave function collapse. Given the low electronic recoil background in the energy region of interest, this allowed to set the most stringent upper limit for the CSL model for correlation lengths of $r_c < 10^{-5}$ m, excluding the parameter space $\lambda/r_c^2 > 3.04 \times 10^{-3}$ s^{-1}m^{-2} at 95% C.L., and the best lower limit on the DP model, excluding regularization scales $R_0 < 1.4 \times 10^{-9}$ m at 95% C.L. By excluding large parts of the CSL parameter space, the results indicate that theoretical extensions of the model, that widen the parameter space, should be in the focus of future experimental tests. The lower limit on the DP model confirms the exclusion of the parameter-free version of the model that was established by previous experiments. The presented study represents the first search for radiation from wave function collapse with a dual-phase TPC and demonstrates the potential of the detection technology beyond the search for dark matter.

XENONnT continues to take data and potentially will achieve an even lower background with an upgraded purification system, enabling more sensitive tests of collapse models. Together with other experiments and technological advances, this will allow further investigation of whether quantum mechanics provides a fundamental description of nature or is merely a method for predicting the outcomes of measurements.

Appendix A

Appendix

Table A.1: Parameters for the selection of ^{83m}Kr event with two distinct S1 signals and one merged S2 signal. The signal from first decay of ^{83m}Kr of 32.1 keV is denoted as $S1_a$ and the signal from the second decay of 9.4 keV as $S1_b$.

Selection
$100 \leq$ Number of contributing PMTs to $S1_a < 200$
$30 \leq$ Number of contributing PMTs to $S1_b < 110$
$10 \leq$ Number of distinct PMTs between $S1_b$ and $S1_a < 60$
$500 \leq$ Delay time between $S1_b$ and $S1_a < 2000$
$S1_a$ width at 90% of the area < 280
if Delay time between S1s < 1500 ns
$\rightarrow$ -0.09 $\times$ Delay time between S1s + 400 $< S1_b$ width at 90% of the area
if Delay time between S1s > 1500 ns $\rightarrow S1_b$ width at 90% of the area <265 ns
$S1_b$ width at 90% of the area < 265 ns

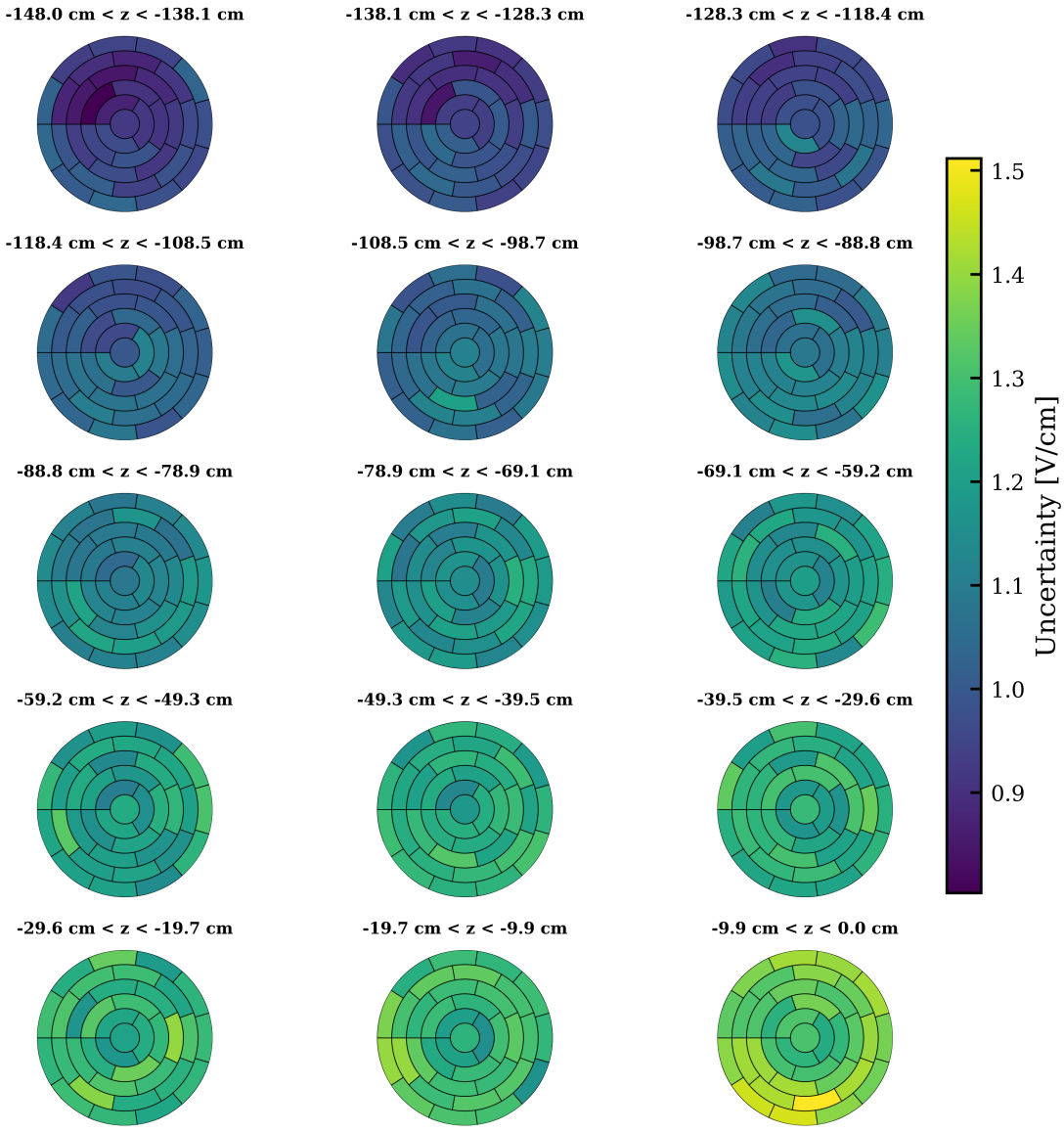

Figure A.1: Map of the statistical uncertainties on the reconstructed drift field strengths in 3D. The map consists of 540 bins in total of equal volume in 15 z-slices.

Acknowledgments

I would like to deeply thank Prof. Dr. Laura Baudis for giving me the opportunity to work on this exciting project and visit the XENONnT detector at LNGS.
I gratefully thank Dr. Christian Wittweg for his continuous guidance, inspiring encouragement, and kind advice. You gave me trust, vision, and motivation while working on this project and you have introduced me to dark matter research showing me broader implications and opportunities.
Further, I would like to thank everyone in the astroparticle physics group for a warm welcome and inclusion into the team and many helpful discussions.
Finally, I would like to thank the entire XENON collaboration for sharing a part of your amazing journey. It was a great pleasure to get to know many of you during the collaboration meeting in Torino or during my shift at LNGS. I am looking forward to hearing about new results of the XENONnT experiment.

Bibliography

[1] A. Bassi et al. Models of Wave-function Collapse, Underlying Theories, and Experimental Tests. *Rev. Mod. Phys.* 85 (2013), pp. 471–527. DOI: 10.1103/RevModPhys.85.471. arXiv: 1204.4325 [quant-ph].

[2] M. Carlesso et al. Present status and future challenges of non-interferometric tests of collapse models. *Nat. Phys.* 18.3 (2022), pp. 243–250. DOI: 10.1038/s41567-021-01489-5. arXiv: 2203.04231 [quant-ph].

[3] E. Aprile et al. Projected WIMP sensitivity of the XENONnT dark matter experiment. *JCAP* 11 (2020), p. 031. DOI: 10.1088/1475-7516/2020/11/031. arXiv: 2007.08796 [physics.ins-det].

[4] E. Aprile et al. Search for New Physics in Electronic Recoil Data from XENONnT. *Phys. Rev. Lett.* 129.16 (2022), p. 161805. DOI: 10.1103/PhysRevLett.129.161805. arXiv: 2207.11330 [hep-ex].

[5] G. C. Ghirardi, P. M. Pearle, and A. Rimini. Markov Processes in Hilbert Space and Continuous Spontaneous Localization of Systems of Identical Particles. *Phys. Rev. A* 42 (1990), pp. 78–79. DOI: 10.1103/PhysRevA.42.78.

[6] L. Diósi. A universal master equation for the gravitational violation of quantum mechanics. *Phys. Lett. A* 120.8 (Mar. 1987), pp. 377–381. DOI: 10.1016/0375-9601(87)90681-5.

[7] E. Schrödinger. Die gegenwärtige Situation in der Quantenmechanik. *Naturwissenschaften* 23.48 (Nov. 1935), pp. 807–812. DOI: 10.1007/BF01491891.

[8] N. Bohr. The Quantum Postulate and the Recent Development of Atomic Theory. *Nature* 121.3050 (1928), pp. 580–590. DOI: 10.1038/121580a0.

[9] J. von Neumann and R. Beyer. *Mathematical Foundations of Quantum Mechanics*. Goldstine Printed Materials. Princeton University Press, 1955. ISBN: 9780691028934. DOI: doi:10.1515/9781400889921.

[10] A. Bassi and G. Ghirardi. A General argument against the universal validity of the superposition principle. *Phys. Lett. A* 275 (2000), p. 373. DOI: 10.1016/S0375-9601(00)00612-5. arXiv: quant-ph/0009020.

[11] A. Bassi. *Philosophy of Quantum Mechanics: Dynamical Collapse Theories*. Feb. 2021. DOI: 10.1093/acrefore/9780190871994.013.77.

[12] T. Maudlin. Three measurement problems. *Topoi* 14 (1995), pp. 7–15.

[13] D. Bohm. A Suggested Interpretation of the Quantum Theory in Terms of "Hidden" Variables. I. *Phys. Rev.* 85 (2 Jan. 1952), pp. 166–179. DOI: 10.1103/PhysRev.85.166.

[14] H. Everett. "Relative State" Formulation of Quantum Mechanics. *Rev. Mod. Phys.* 29 (3 July 1957), pp. 454–462. DOI: 10.1103/RevModPhys.29.454.

[15] G. C. Ghirardi, A. Rimini, and T. Weber. A Unified Dynamics for Micro and MACRO Systems. *Phys. Rev. D* 34 (1986), p. 470. DOI: 10.1103/PhysRevD.34.470.

[16] A. Bassi. Models of spontaneous wave function collapse: what they are, and how they can be tested. *J. Phys. Conf. Ser.* 701 (Mar. 2016), p. 012012. DOI: 10.1088/1742-6596/701/1/012012.

[17] L. Arnold. Stochastic differential equations. *New York* (1974).

[18] S. L. Adler. Lower and Upper Bounds on CSL Parameters from Latent Image Formation and IGM Heating. *J. Phys. A* 40 (2007). [Erratum: J.Phys.A 40, 13501 (2007)], pp. 2935–2958. DOI: 10.1088/1751-8113/40/12/S03. arXiv: quant-ph/0605072.

[19] A. Smirne and A. Bassi. Dissipative Continuous Spontaneous Localization (CSL) model. *Sci. Rep.* 5, 12518 (Aug. 2015), p. 12518. DOI: 10.1038/srep12518. arXiv: 1408.6446 [quant-ph].

[20] S. L. Adler and A. Bassi. Collapse models with non-white noises. *J. Phys. A Math. Theor.* 40.50 (Nov. 2007), pp. 15083–15098. DOI: 10.1088/1751-8113/40/50/012.

[21] S. L. Adler. *Quantum Theory as an Emergent Phenomenon: The Statistical Mechanics of Matrix Models as the Precursor of Quantum Field Theory*. Cambridge University Press, 2004. DOI: 10.1017/CBO9780511535277.

[22] R. Penrose. On gravity's role in quantum state reduction. *Gen. Rel. Grav.* 28 (1996), pp. 581–600. DOI: 10.1007/BF02105068.

[23] R. Penrose. On the Gravitization of Quantum Mechanics 1: Quantum State Reduction. *Found. Phys.* 44 (2014). Ed. by F. Scardigli and M. Nespoli, pp. 557–575. DOI: 10.1007/s10701-013-9770-0.

[24] M. Arndt and K. Hornberger. Testing the limits of quantum mechanical superpositions. *Nat. Phys.* 10.4 (Apr. 2014), pp. 271–277. DOI: 10.1038/nphys2863. arXiv: 1410.0270 [quant-ph].

[25] Y. Y. Fein et al. Quantum superposition of molecules beyond 25 kDa. *Nat. Phys.* 15.12 (Sept. 2019), pp. 1242–1245. DOI: 10.1038/s41567-019-0663-9.

[26] M. Toroš, G. Gasbarri, and A. Bassi. Colored and dissipative continuous spontaneous localization model and bounds from matter-wave interferometry. *Phys. Lett. A* 381.47 (Dec. 2017), pp. 3921–3927. DOI: 10.1016/j.physleta.2017.10.002. arXiv: 1601.03672 [quant-ph].

[27] M. Toroš and A. Bassi. Bounds on quantum collapse models from matter-wave interferometry: calculational details. *J. Phys. A Math.* 51.11, 115302 (Mar. 2018), p. 115302. DOI: 10.1088/1751-8121/aaabc6.

[28] M. Bilardello et al. Bounds on collapse models from cold-atom experiments. *Phys. A: Stat. Mech. Appl.* 462 (Nov. 2016), pp. 764–782. DOI: 10.1016/j.physa.2016.06.134. arXiv: 1605.01891 [quant-ph].

[29] M. Carlesso et al. Non-interferometric test of the continuous spontaneous localization model based on rotational optomechanics. *New J. Phys.* 20.8 (2018), p. 083022. DOI: 10.1088/1367-2630/aad863. arXiv: 1708.04812 [quant-ph].

[30] M. Armano et al. Beyond the Required LISA Free-Fall Performance: New LISA Pathfinder Results down to 20 μHz. *Phys. Rev. Lett.* 120 (6 Feb. 2018), p. 061101. DOI: 10.1103/PhysRevLett.120.061101.

[31] A. Vinante et al. Narrowing the Parameter Space of Collapse Models with Ultracold Layered Force Sensors. *Phys. Rev. Lett.* 125.10, 100404 (Sept. 2020), p. 100404. DOI: 10.1103/PhysRevLett.125.100404. arXiv: 2002.09782 [quant-ph].

[32] C. Alduino et al. The projected background for the CUORE experiment. *Eur. Phys. J. C* 77.8, 543 (Aug. 2017), p. 543. DOI: 10.1140/epjc/s10052-017-5080-6.

[33] S. Donadi et al. Novel CSL bounds from the noise-induced radiation emission from atoms. *Eur. Phys. J. C* 81.8 (2021), p. 773. DOI: 10.1140/epjc/s10052-021-09556-0. arXiv: 2107.11237 [quant-ph].

[34] I. J. Arnquist et al. Search for Spontaneous Radiation from Wave Function Collapse in the Majorana Demonstrator. *Phys. Rev. Lett.* 129 (8 Aug. 2022), p. 080401. DOI: 10.1103/PhysRevLett.129.080401.

[35] S. L. Adler and A. Vinante. Bulk heating effects as tests for collapse models. *Phys. Rev. A* 97.5, 052119 (May 2018), p. 052119. DOI: 10.1103/PhysRevA.97.052119. arXiv: 1801.06857 [quant-ph].

[36] B. Helou et al. LISA pathfinder appreciably constrains collapse models. *Phys. Rev. D* 95.8, 084054 (Apr. 2017), p. 084054. DOI: 10.1103/PhysRevD.95.084054. arXiv: 1606.03637 [quant-ph].

[37] M. Carlesso, L. Ferialdi, and A. Bassi. Colored collapse models from the non-interferometric perspective. *Eur. Phys. J. D* 72.9, 159 (Sept. 2018), p. 159. DOI: 10.1140/epjd/e2018-90248-x. arXiv: 1805.10100 [quant-ph].

[38] S. Donadi et al. Underground test of gravity-related wave function collapse. *Nat. Phys.* 17.1 (2021), pp. 74–78. DOI: 10.1038/s41567-020-1008-4. arXiv: 2111.13490 [quant-ph].

[39] E. Aprile et al. The XENON1T Dark Matter Experiment. *Eur. Phys. J. C* 77.12 (2017), p. 881. DOI: 10.1140/epjc/s10052-017-5326-3. arXiv: 1708.07051 [astro-ph.IM].

[40] R. L. Workman et al. Review of Particle Physics. 26. Dark Matter. *PTEP* 2022 (2022), p. 083C01. DOI: 10.1093/ptep/ptac097.

[41] L. Roszkowski, E. M. Sessolo, and S. Trojanowski. WIMP dark matter candidates and searches—current status and future prospects. *Rept. Prog. Phys.* 81.6 (2018), p. 066201. DOI: 10.1088/1361-6633/aab913. arXiv: 1707.06277 [hep-ph].

[42] E. Aprile et al. Material radiopurity control in the XENONnT experiment. *Eur. Phys. J. C* 82.7 (2022), p. 599. DOI: 10.1140/epjc/s10052-022-10345-6. arXiv: 2112.05629 [physics.ins-det].

[43] M. Murra et al. Design, construction and commissioning of a high-flow radon removal system for XENONnT (May 2022). arXiv: 2205.11492 [physics.ins-det].

[44] E. Aprile et al. Removing krypton from xenon by cryogenic distillation to the ppq level. *Eur. Phys. J. C* 77.5 (2017), p. 275. DOI: 10.1140/epjc/s10052-017-4757-1. arXiv: 1612.04284 [physics.ins-det].

[45] E. Aprile et al. Conceptual design and simulation of a water Cherenkov muon veto for the XENON1T experiment. *JINST* 9 (2014), P11006. DOI: 10.1088/1748-0221/9/11/P11006. arXiv: 1406.2374 [astro-ph.IM].

[46] P. Barrow et al. Qualification Tests of the R11410-21 Photomultiplier Tubes for the XENON1T Detector. *JINST* 12.01 (2017), P01024. DOI: 10.1088/1748-0221/12/01/P01024. arXiv: 1609.01654 [astro-ph.IM].

[47] E. Aprile and T. Doke. Liquid Xenon Detectors for Particle Physics and Astrophysics. *Rev. Mod. Phys.* 82 (2010), pp. 2053–2097. DOI: 10.1103/RevModPhys.82.2053. arXiv: 0910.4956 [physics.ins-det].

[48] K. Fujii et al. High-accuracy measurement of the emission spectrum of liquid xenon in the vacuum ultraviolet region. *Nucl. Instrum. Methods Phys. Res. A* 795 (Sept. 2015), pp. 293–297. DOI: 10.1016/j.nima.2015.05.065.

[49] E. Aprile et al. XENON1T Dark Matter Data Analysis: Signal Reconstruction, Calibration and Event Selection. *Phys. Rev. D* 100.5 (2019), p. 052014. DOI: 10.1103/PhysRevD.100.052014. arXiv: 1906.04717 [physics.ins-det].

[50] H. Schulze Eißing. "Energy calibration of XENONnT". XENONnT collaboration internal note. 2022.

[51] J. R. Angevaare et al. *XENONnT/straxen: v1.7.2*. Version v1.7.2. July 2022. DOI: 10.5281/zenodo.6881647.

[52] J. Aalbers et al. *AxFoundation/strax: v1.3.0*. Version v1.3.0. Sept. 2022. DOI: 10.5281/zenodo.7064111.

[53] *Straxen datastructure*. URL: https://straxen.readthedocs.io/en/latest/reference/datastructure_nT.html. (accessed: 11.10.2022).

[54] D. S. Akerib et al. ^{83m}Kr calibration of the 2013 LUX dark matter search. *Phys. Rev. D* 96.11 (2017), p. 112009. DOI: 10.1103/PhysRevD.96.112009. arXiv: 1708.02566 [physics.ins-det].

[55] V. Hannen et al. Limits on the release of Rb isotopes from a zeolite based 83mKr calibration source for the XENON project. *JINST* 6.10 (Oct. 2011), P10013. DOI: 10.1088/1748-0221/6/10/P10013.

[56] M. Pierre. "^{83m}Kr event selection". XENONnT collaboration internal note. 2022.

[57] E. Aprile et al. Energy resolution and linearity of XENON1T in the MeV energy range. *Eur. Phys. J. C* 80.8 (2020), p. 785. DOI: 10.1140/epjc/s10052-020-8284-0. arXiv: 2003.03825 [physics.ins-det].

[58] J. Long. "S2 correction in XENONnT". XENONnT collaboration internal note. 2022.

[59] E. Aprile et al. XENON1T dark matter data analysis: Signal and background models and statistical inference. *Phys. Rev. D* 99.11 (2019), p. 112009. DOI: 10.1103/PhysRevD.99.112009. arXiv: 1902.11297 [physics.ins-det].

[60] G. Plante et al. Liquid-phase purification for multi-tonne xenon detectors. *Eur. Phys. J. C* 82.10 (2022), p. 860. DOI: 10.1140/epjc/s10052-022-10832-w. arXiv: 2205.07336 [physics.ins-det].

[61] F. Toschi and R. Peres. "Electric field simulation". XENONnT collaboration internal note. 2022.

[62] COMSOL AB, Stockholm, Sweden, COMSOL Multiphysics.

[63] M. Szydagis et al. *Noble Element Simulation Technique*. Version v2.3.11. Sept. 2022. DOI: 10.5281/zenodo.7061832.

[64] M. Szydagis et al. NEST: a comprehensive model for scintillation yield in liquid xenon. *JINST* 6.10 (Oct. 2011), P10002–P10002. DOI: 10.1088/1748-0221/6/10/p10002.

[65] F. Jörg et al. Characterization of alpha and beta interactions in liquid xenon. *Eur. Phys. J. C* 82.4 (2022), p. 361. DOI: 10.1140/epjc/s10052-022-10259-3. arXiv: 2109.13735 [physics.ins-det].

[66] S. Andaloro et al. *NESTCollaboration/nestpy:* version 1.4.9. June 2021. DOI: 10.5281/zenodo.4897887.

[67] L. Baudis et al. Response of liquid xenon to Compton electrons down to 1.5 keV. *Phys. Rev. D* 87.11 (2013), p. 115015. DOI: 10.1103/PhysRevD.87.115015. arXiv: 1303.6891 [astro-ph.IM].

[68] A. G. Singh et al. Analysis of ^{83m}Kr prompt scintillation signals in the PIXeY detector. *JINST* 15.01 (2020), P01023. DOI: 10.1088/1748-0221/15/01/P01023. arXiv: 1911.03999 [physics.ins-det].

[69] Y. Ma. "XENONnT data-driven electric field". XENONnT collaboration internal note. 2022.

[70] Q. Fu. Spontaneous radiation of free electrons in a nonrelativistic collapse model. *Phys. Rev. A* 56 (3 Sept. 1997), pp. 1806–1811. DOI: 10.1103/PhysRevA.56.1806.

[71] T. Prohaska et al. *Pure Appl. Chem.* 94.5 (2022), pp. 573–600. DOI: doi:10.1515/pac-2019-0603.

[72] S. Agostinelli et al. GEANT4–a simulation toolkit. *Nucl. Instrum. Meth. A* 506 (2003), pp. 250–303. DOI: 10.1016/S0168-9002(03)01368-8.

[73] E. Aprile et al. Excess electronic recoil events in XENON1T. *Phys. Rev. D* 102.7 (2020), p. 072004. DOI: 10.1103/PhysRevD.102.072004. arXiv: 2006.09721 [hep-ex].

[74] M. Agostini et al. Comprehensive measurement of *pp*-chain solar neutrinos. *Nature* 562.7728 (2018), pp. 505–510. DOI: 10.1038/s41586-018-0624-y.

[75] J. Ye. "Statistical inference for the low energy electric recoil analysis in XENONnT." XENONnT collaboration internal note. 2022.

[76] R. L. Workman et al. Review of Particle Physics. 40. Statistics. *PTEP* 2022 (2022), p. 083C01. DOI: 10.1093/ptep/ptac097.

[77] S. S. Wilks. The Large-Sample Distribution of the Likelihood Ratio for Testing Composite Hypotheses. *Ann. Math. Stat.* 9.1 (1938), pp. 60–62. DOI: 10.1214/aoms/1177732360.